



ELSEVIER

Contents lists available at [ScienceDirect](https://www.sciencedirect.com)

Journal of the Mechanics and Physics of Solids

journal homepage: www.elsevier.com/locate/jmps

Elastic wetting: Substrate-supported droplets confined by soft elastic membranes

Yifan Rao^{a,1}, Shutao Qiao^{a,1}, Zhaohu Dai^a, Nanshu Lu^{a,b,c,d,*}^a Center for Mechanics of Solids, Structures and Materials, Department of Aerospace Engineering and Engineering Mechanics, The University of Texas at Austin, 2501 Speedway, EER 7.614B, TX 78712, United States^b Department of Mechanical Engineering, The University of Texas at Austin, TX 78712, United States^c Department of Biomechanical Engineering, The University of Texas at Austin, TX 78712, United States^d Texas Material Institute, The University of Texas at Austin, TX 78712, United States

ARTICLE INFO

Keywords:

Elastic wetting
Contact angle
Surface tension
Elasto-capillarity
Bulge test
Blister

ABSTRACT

While classical wetting is well captured by the famous Young's equation and classical bulge and blister models are readily available, there is limited understanding of a micro- or nano-scale droplet being covered by an ultrasoft elastic membrane. We call this phenomenon *elastic wetting* to feature the interplay between the liquid's surface tension and the membrane's elastic deformation. Examples of elastic wetting include cell blebs and 2D material bubbles, where the membrane thickness ranges from microns to sub-nanometers. In this work, we study the equilibrium of elastic wetting and solve for the profiles and the pressure-volume relations of the membrane-confined droplets. We show that in elastic wetting, the pressure across the membrane/droplet interface can be described by a simple superposition of the Young-Laplace equation and the nonlinear membrane equation. Furthermore, nonlinear elasticity, geometric nonlinearity, and surface tension, together with membrane-substrate adhesion, interweave at the contact line, leading to rich membrane-confined droplet configurations. Finally, we examine the effect of substrate compliance on elastic wetting and find that the rigid substrate assumption approximates well for most of the existing experiments in the literature. Our results provide fundamental mechanistic insights into the various phenomena of elastic wetting as well as viable means to extract physical parameters including the bubble pressure and the interface energies.

1. Introduction

Wetting is an everyday phenomenon that refers to how a liquid droplet adheres to a solid surface (De Gennes et al., 2013). When surface tension dominates other forces, such as gravity, droplets on rigid substrates form in the shape of a spherical cap (except the limiting case of complete wetting where the liquid spreads out). The degree of wetting, i.e. *wettability*, is characterized by the *contact angle* of this liquid spherical cap, which is size-independent, described by Young's equation (Young, 1805), and measured at the liquid-vapor-solid interface, which is called the *contact line*. Conventionally, contact angles are widely measured for the quantification of solid surface tensions (Kwok et al., 1998; Shimizu and Demarquette, 2000; Wu, 1971). In recent years, many new efforts focused on how the wettability (or the drop geometry) can be tuned. Examples include the design of the self-cleaning surfaces (Blossey, 2003) and

* Corresponding author.

E-mail address: nanshulu@utexas.edu (N. Lu).¹ Equal contribution.<https://doi.org/10.1016/j.jmps.2021.104399>

Received 7 August 2020; Received in revised form 11 March 2021; Accepted 12 March 2021

Available online 14 March 2021

0022-5096/© 2021 Elsevier Ltd. All rights reserved.

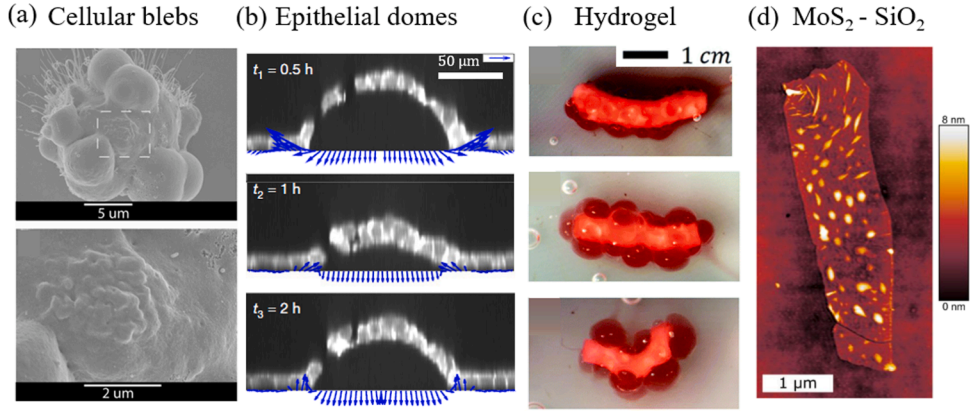


Fig. 1. Examples of elastic wetting in experiments. (a) Scanning electron micrographs (SEM) of a blebbing filamin-deficient cell (Charras, 2008). (b) Epithelial domes generated on a soft elastomer substrate driven by transmural pressure (Latorre et al., 2018). (c) Blisters appear when temperature-sensitive hydrogels transit from swollen to unswollen phase (Shen et al., 2019). (d) Liquid nano-bubbles formed spontaneously when exfoliating a monolayer MoS₂ on a SiO₂ substrate (Sanchez et al., 2018).

Table 1

Experimentally relevant parameters and their nondimensionalization for elastic wetting. Substrate-supported droplets are widely observed to be confined by thin membranes of biological materials (Latorre et al., 2018), soft polymers (Gilcreest et al., 2004; Shen et al., 2019; Xia et al., 2019), and 2D materials (Ghorbanfekr-Kalashami et al., 2017; Khestanova et al., 2016; Sanchez et al., 2018; Wang et al., 2009). In this table, h is the central height of the blister, R_0 is the base radius of the blister, h/R_0 is hence the aspect ratio of the blister, t_0 is the thickness of the membrane, μ is the shear modulus of the membrane, γ_{lm} is the energy density of the liquid-membrane interface, $\alpha = \frac{\gamma_{lm}}{\mu t_0}$ is the elasto-capillary number (see Eq. (25)), $\frac{\alpha}{(h/R_0)^2}$ is adopted to quantify the ratio of interface energy to elastic energy, μ_s is the shear modulus of the substrate, and $\frac{\mu t_0}{\mu_s R_0}$ is used for substrate rigidity evaluation.

	Biological materials	Soft polymers	2D materials
h (m)	$10^{-6} \sim 10^{-5}$	$10^{-4} \sim 10^{-3}$	$10^{-9} \sim 10^{-8}$
R_0 (m)	$\sim 10^{-5}$	$\sim 10^{-3}$	$\sim 10^{-7}$
h/R_0	$0.1 \sim 1$	$0.1 \sim 1$	$0.02 \sim 0.2$
t_0 (m)	$\sim 10^{-6}$	$\sim 10^{-5}$	$\sim 10^{-9}$
μ (Pa)	$\sim 10^3$	$\sim 10^5$	$\sim 10^{11}$
γ_{lm} (N/m)	$\sim 10^{-3}$	$\sim 10^{-2}$	$\sim 10^{-2}$
$\alpha = \frac{\gamma_{lm}}{\mu t_0}$	~ 1	$\sim 10^{-2}$	$\sim 10^{-4}$
$\frac{\alpha}{(h/R_0)^2}$	$1 \sim 10^2$	$10^{-2} \sim 1$	$10^{-3} \sim 1$
μ_s (Pa)	$\sim 10^3$	$\sim 10^5$	$\sim 10^{10}$
$\frac{\mu t_0}{\mu_s R_0}$	$\sim 10^{-1}$	$\sim 10^{-2}$	$\sim 10^{-1}$

the control of nanoprintings (Fernández-Toledano et al., 2020).

Recent experiments reported a slightly different wetting phenomenon where the droplets were confined by ultrasoft (i.e. ultrathin or ultracompliant or both) elastic membranes (see Fig. 1). It has been found in many different material systems with the membrane thickness ranging from microns to sub-nanometers. Examples include cellular blebs (i.e., the protrusion of cell membrane) (Fig. 1a) (Charras, 2008; Dimova and Lipowsky, 2012), epithelial domes on an elastomer (Fig. 1b) (Latorre et al., 2018), the blistering of thermosensitive hydrogel (Fig. 1c) (Shen et al., 2019), and the nano-bubbles at 2D material interfaces (Fig. 1d) (Sanchez et al., 2021, 2018). We call this phenomenon *elastic wetting* because the elasticity of the membrane and the surface tension of the liquid together govern the wetting behavior.

Elastic wetting involves liquid bulging an elastic membrane, which is reminiscent of classical blister tests – a popular setup to measure the elastic and adhesive properties of thin films (Dannenberg, 1961; Vlassak and Nix, 1992). A major difference is that the classical models of blister tests typically neglect the surface tension of the liquid (Gent and Lewandowski, 1987; Jensen, 1991; Xiang et al., 2005). As a consequence, blisters pressurized by either gas or liquid would lead to identical measures of material properties, such as the stiffness of the film and the film-substrate interface adhesion (Cao et al., 2015, 2014; Hohlfelder et al., 1996; Wang et al., 2013; Yue et al., 2012).

As the film thickness and modulus decrease, the elastic energy drops to a level comparable with or even lower than the surface/interface energies, which we refer to as elastic wetting (Fig. 1). In this scenario, the behavior of the blister would depend on the specific

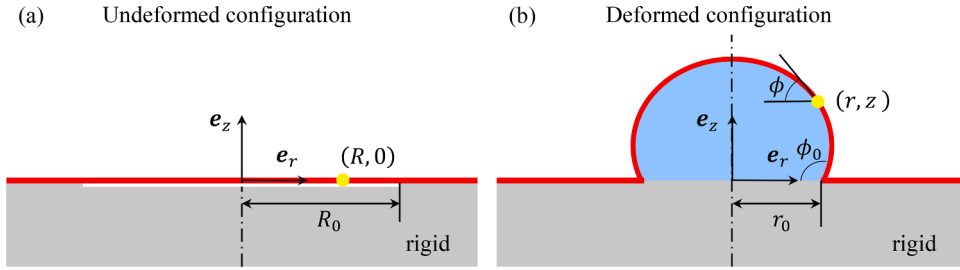


Fig. 2. An axisymmetric droplet trapped between a rigid substrate (gray) and a thin elastic membrane (red): (a) the undeformed configuration, (b) the deformed configuration.

type of liquid. Experimentally, it has been observed that the aspect ratio (i.e., height-to-radius ratio) of the droplet trapped between monolayer graphene and a graphite substrate could increase by $\sim 40\%$ as the droplet substance changed from ethanol to water (Ghorbanfekr-Kalashami et al., 2017). The aspect ratio of such elastically confined droplets has been proved to be also an indicator of the membrane-substrate adhesion (Dai et al., 2019; Sanchez et al., 2018). In this work, we focus on elastic wetting problems in which the droplet is supported by a substrate while confined by an ultrasoft elastic membrane. We note that there also exist a number of other interesting phenomena in the literature that may share similar physical ingredients of the elastic wetting, such as droplets being confined by an elastic capsule (Knoche et al., 2013), being supported by a suspended membrane (Davidovitch and Vella, 2018; Liu et al., 2020), and being sandwiched by elastic membranes (Schulman and Dalnoki-Veress, 2018).

Despite increasing experimental observations of elastic wetting (Fig. 1), there is no complete theoretical framework to offer quantitative understanding and prediction. As a result, a number of fundamental questions remain unanswered: How does the membrane elasticity perturb the Young-Laplace equation built for *sessile drops* (i.e. classical wetting where droplets are supported by a substrate without membrane coverage)? How does the thin confining membrane modify the contact line previously described by the Young's equation? When can the substrate be considered rigid? These natural questions would be more intriguing for the membrane-confined droplets with large aspect ratios, e.g. 0.2 (to be addressed in discussions), when both material and geometric nonlinearities set in. Blisters with large aspect ratios indeed have been widely observed in experiments. Table 1 summarizes the possible scales of parameters pertinent to elastic wetting, including the central height of the blister, h , the base radius of the blister, R_0 , and the corresponding aspect ratio, h/R_0 . When droplets are confined under biological or soft polymer membranes, the maximum aspect ratio could reach ~ 1 (Charras, 2008; Latorre et al., 2018; Shen et al., 2019). For bubbles trapped on 2D material interfaces, the maximum aspect ratio approaches 0.2 when the interface adhesion is strong (Dai et al., 2020a; Ghorbanfekr-Kalashami et al., 2017; Khestanova et al., 2016). Other parameters in Table 1 will be discussed later.

To answer those fundamental questions and to achieve quantitative predictions, we present a fully-coupled theoretical framework for elastic wetting, which contains the large deformation, the material nonlinearity, the interface energies as well as various interfacial constraints. We show that in elastic wetting, the pressure difference across the membrane/droplet interface can be described by a simple superposition of the Young-Laplace equation and the nonlinear membrane equation. Dimensionless governing parameters emerge naturally during the derivation. We discover that the interplay of nonlinear elasticity, geometric nonlinearity, and interfacial tension, together with membrane-substrate adhesion, leads to surprisingly rich elastic wetting configurations. We demonstrate that this understanding could potentially be used to determine liquid-membrane interface energy and the membrane-substrate adhesion energy.

This paper is arranged as follows. In Section 2, we establish the theoretical formulation for elastic wetting on a rigid substrate. In Section 3, we demonstrate an imaginary case of elastic wetting with a roller boundary that can successfully decay to the sessile drop scenario when the membrane stiffness vanishes. In Section 4, we unveil the quasi-static growth of a membrane-confined droplet with or without interfacial slippage by comparing three different boundary conditions: clamped, adhesive, and slippery boundaries. Section 5 discusses the effects of substrate compliance and the applicability of our nonlinear theory of elastic wetting, followed by concluding remarks.

2. Theoretical formulation

This section provides the complete formulation for the boundary value problem of elastic wetting in the order of kinematics, equilibrium, constitutive law, and boundary conditions.

2.1. Kinematics

We consider an axisymmetric droplet trapped by an isotropic thin elastic membrane on a rigid substrate. The blistering process is modeled as a flat thin membrane with an initial thickness t_0 being inflated by incompressible liquid. A coordinate system (e_r, e_z) is introduced, with its origin located at the center of the undeformed membrane. The thin membrane assumption warrants the same profile of the droplet and the membrane. Fig. 2 offers the schematics for undeformed and deformed configurations. In the undeformed configuration (Fig. 2a), the membrane is assumed to be stress-free, and each material point can be labeled by $(R, 0)$. In the deformed

configuration (Fig. 2b), the blister profile can be specified by the radius $r(R)$, the height $z(R)$, and the thickness $t(R)$. The edge of the blister, i.e. the location of the contact line, is specified by $(r_0, 0)$, which corresponds to $(R_0, 0)$ in the undeformed configuration, i.e., $r_0 = r(R_0)$.

Let λ_r , λ_θ and λ_t denote the principal stretches of the membrane along the radial, hoop, and thickness directions, respectively, we have

$$\lambda_r = \sqrt{r'^2 + z'^2}, \quad \lambda_\theta = \frac{r}{R}, \quad \lambda_t = \frac{t}{t_0}, \tag{1}$$

where (\prime) represents $d(\)/dR$. As shown in Fig. 2b, $\phi(R)$ is the slope of the deformed blister profile at the location (r, z) , satisfying

$$\sin\phi = -\frac{z'}{\lambda_r}, \quad \cos\phi = \frac{r'}{\lambda_r}. \tag{2}$$

Moreover, $\phi_0 = \phi(R_0)$ is the contact angle of the droplet under the elastic confinement, which we call the *elastic wetting contact angle*.

Assuming the membrane is incompressible (e.g. elastomers), i.e., $\lambda_r\lambda_\theta\lambda_t = 1$, the thickness of the deformed membrane is

$$t = \frac{t_0}{\lambda_r\lambda_\theta}. \tag{3}$$

Elastic wetting with compressible membranes can be further investigated by considering the Poisson's effect. However, it is expected to share very similar features with incompressible membranes in terms of blister profiles. The two situations should only differ quantitatively as illustrated in Sanchez et al.'s work that derived the aspect ratios of 2D material confined bubbles for different Poisson's ratios (Sanchez et al., 2018).

The area of the liquid-membrane interface in the deformed configuration is

$$A_1 = \int_0^{R_0} 2\pi r \sqrt{r'^2 + z'^2} dR, \tag{4}$$

the area of the liquid-substrate interface is

$$A_2 = \pi r_0^2 = \int_0^{R_0} 2\pi r r' dR, \tag{5}$$

the area of the membrane-substrate interface is

$$A_3 = \int_{R_0}^{\infty} 2\pi r r' dR, \tag{6}$$

and the volume of the membrane-confined droplet is

$$V = \int_0^{R_0} 2\pi r r' z dR. \tag{7}$$

2.2. Equilibrium equations

Taking both elastic and interface energies into consideration, the total free energy of the elastic wetting problem can be written as

$$\Pi = U_m - \Delta p V + \gamma_{lm} A_1 + \gamma_{ls} A_2 + \gamma_{ms} A_3, \tag{8}$$

where U_m is the strain energy due to the stretching of the membrane, Δp is the inner pressure of the droplet, γ_{lm} , γ_{ls} and γ_{ms} are the energy densities of the liquid-membrane interface, the liquid-substrate interface, and the membrane-substrate interface, respectively. We neglect the gravity of the liquid here due to the small-scale nature of the elastic wetting problem, though the gravity, as well as other external potentials (e.g., electrical potential) (Zhao and Suo, 2008; Zhu et al., 2010), could be readily added to Eq. (8) (Bico et al., 2018; Roman and Bico, 2010). In this paper, all three interface energy densities are assumed to be constant, i.e., independent of the deformation of the materials, which is expected to be true for amorphous elastomers (Schulman et al., 2018). Some polymeric materials have time-dependent surface/interface tensions due to the remodeling of the polymer chains on surfaces (Yasuda et al., 1981). However, we do not consider such complexity here so that the simplified theoretical setting would allow for the exploration of some critical features of quasi-static elastic wetting systems. For crystalline membranes (e.g., 2D materials), although their strain-dependent surface energies were investigated by considering the Shuttleworth effect (Shuttleworth, 1950), such effect could still be neglected in our elastic wetting analysis because most blisters confined by 2D materials have relatively small aspect ratios (see Table 1) and hence

small strains in the membranes ($< \sim 2\%$).

Combining with Eq. (1), the membrane energy U_m can be computed by

$$U_m = \int_0^{R_0} 2\pi t_0 RW(r, r', z') dR + \int_{R_0}^{\infty} 2\pi t_0 RW(r, r') dR, \tag{9}$$

where $W = W(\lambda_r, \lambda_\theta)$ is the strain energy per unit volume in the undeformed configuration of the membrane. The second term on the right side of Eq. (9) accounts for the membrane energy outside of the membrane-confined droplet where $z = z' = 0$. This term would be zero when the membrane is clamped along the contact line. However, for droplets confined by atomically smooth 2D materials (one of the cases that will be discussed in Section 4), the membrane could slide on the substrate with negligible shear resistance such that this term is no longer zero (Wang et al., 2017b).

Substituting Eqs. (4)-(7) and (9) into Eq. (8), one can perform variations of the total free energy Π with respect to r, z, r', z' . At equilibrium, the principle of minimum free energy is applied, i.e.,

$$\delta\Pi = 0, \tag{10}$$

which leads to equilibrium equations

$$\begin{cases} \kappa_r N_r + \kappa_\theta N_\theta + \gamma_{lm}(\kappa_r + \kappa_\theta) + \Delta p = 0 \\ \frac{dN_r}{dR} + \frac{r'(N_r - N_\theta)}{r} = 0 \end{cases} \quad \forall 0 \leq R < R_0, \tag{11}$$

and

$$\begin{cases} z = 0 \\ \frac{dN_r}{dR} + \frac{r'(N_r - N_\theta)}{r} = 0 \end{cases} \quad \forall R \geq R_0. \tag{12}$$

We use κ_r and κ_θ to denote the principal curvatures in the directions of the principal stretches λ_r and λ_θ , respectively:

$$\kappa_r = \frac{r'z'' - r''z'}{(r'^2 + z'^2)^{3/2}}, \quad \kappa_\theta = \frac{z'}{r(r'^2 + z'^2)^{1/2}}. \tag{13}$$

N_r and N_θ are in-plane radial and hoop membrane tensions, respectively, which could be related to the in-plane Cauchy stresses of the membrane, σ_r and σ_θ , through

$$N_r = t\sigma_r = \frac{t_0}{\lambda_\theta} \frac{\partial W}{\partial \lambda_r}, \quad N_\theta = t\sigma_\theta = \frac{t_0}{\lambda_r} \frac{\partial W}{\partial \lambda_\theta}, \tag{14}$$

where $\sigma_r = \lambda_r(\partial W / \partial \lambda_r)$ and $\sigma_\theta = \lambda_\theta(\partial W / \partial \lambda_\theta)$.

2.3. Constitutive law

The normal equilibrium in Eq. (11) indicates that the pressure difference across the liquid-membrane interface is a simple summation of pressures due to membrane tension (via a nonlinear membrane theory) and interfacial tension (via Young-Laplace equation). Unlike the uniform interfacial tension, the membrane tension varies spatially, depending on the local stretches as well as the constitutive law of the membrane, as delineated in Eq. (14). This motivates us to investigate the effect of different material behaviors on elastic wetting. To do so, both neo-Hookean and Gent material models are adopted in this paper. The neo-Hookean model (Rivlin and Taylor, 1948) provides a mathematically simple constitutive law for the nonlinear behavior of isotropic polymers such as elastomers. The strain energy density is given by

$$W = \frac{\mu}{2} \left(\lambda_r^2 + \lambda_\theta^2 + \frac{1}{\lambda_r^2 \lambda_\theta^2} - 3 \right), \tag{15}$$

where μ is the shear modulus of the membrane. When the length of each polymer chain approaches its finite contour length, the following Gent model (Gent, 1996, 2005) captures a strain hardening phenomenon

$$W = -\frac{\mu}{2} J_m \ln \left(1 - \frac{I_1 - 3}{J_m} \right), \tag{16}$$

where J_m is a material constant related to the limiting stretch of the membrane and I_1 is the first invariant of the left Cauchy-Green deformation tensor. It is obvious that the neo-Hookean model is a special case of the Gent model when $J_m \rightarrow \infty$.

Table 2
Illustration and mathematical description of the sessile drop and the membrane-confined droplet with four different boundary conditions.

	Droplet	Sliding	Clamped	Adhesive	Slippery
Schematic					
Contact angle	$\cos\phi_Y = \frac{\gamma_s - \gamma_{ls}}{\gamma_l}$	$\cos\phi_0 = \frac{\gamma_s - \gamma_{ls}}{N_r^- + \gamma_{lm}}$	Arbitrary	$\cos\phi_0 = \frac{\gamma_{ms} - \gamma_{ls} + \lambda_r^- N_r^- - t_0 W^-}{N_r^- + \gamma_{lm}}$	$\cos\phi_0 = \frac{\gamma_{ms} - \gamma_{ls} + N_r^+}{N_r^- + \gamma_{lm}}$
Variation constraint	Prescribed volume	$R_0 = \text{const}$ $r_0 \neq \text{const}$	$R_0 = r_0 = \text{const}$	$R_0 = r_0 \neq \text{const}$	$R_0 \neq \text{const}$ $r_0 \neq \text{const}$
Controlling numbers	$\alpha = \frac{\gamma_l}{\mu t_0} \rightarrow \infty; \beta = \frac{\gamma_s - \gamma_{ls}}{\gamma_l}$	$\alpha = \frac{\gamma_{lm}}{\mu t_0}; \beta = \frac{\gamma_s - \gamma_{ls}}{\gamma_{lm}}$	$\alpha = \frac{\gamma_{lm}}{\mu t_0}$	$\alpha = \frac{\gamma_{lm}}{\mu t_0}; \beta = \frac{\gamma_{ms} - \gamma_{ls}}{\gamma_{lm}}$	$\alpha = \frac{\gamma_{lm}}{\mu t_0}; \beta = \frac{\gamma_{ms} - \gamma_{ls}}{\gamma_{lm}}$

2.4. Contact line (boundary conditions)

Having shown that in the elastic wetting problem, the Young-Laplace equation is modified by the addition of a nonlinear membrane theory, we further demonstrate a plethora of complexities emerging at the contact line due to the existence of membrane. The boundary terms generated when proceeding Eq. (10) constitute boundary conditions for the elastic wetting problem. The details of the derivation are tedious and presented in Appendix A. Here, we discuss the general conclusions in brief.

At the contact line of the blister $r_0 = r(R_0)$, $r(R)$ and $z(R)$ are continuous, while $r'(R)$ and $z'(R)$ can be discontinuous. To describe different continuity conditions, we use $(x)^-$ and $(x)^+$ to represent x evaluated on the left (inner) and right (outer) sides of $R = R_0$, respectively. In addition, the initial radius of the contact line R_0 could have nonzero variation, i.e., $\delta R_0 \neq 0$, when the membrane-substrate interfacial delamination propagates. Therefore, the variation of the evaluation of a function $f(R)$ at $R = R_0$ (i.e., $\delta f(R_0)$) could be different from the evaluation of the variation of this function (i.e., $(\delta f)(R_0)$). In particular, $(\delta f)(R_0) = \delta f(R_0) - f'(R_0)\delta R_0$. Based on the grounds, the boundary terms derived from Eq. (10) are expressed as (also see Appendix A for details)

$$\begin{aligned}
 & [\cos\phi^-(N_r^- + \gamma_{lm}) - \Delta p z_0 + (\gamma_{ls} - \gamma_{ms}) - \cos\phi^+ N_r^+] r_0 \delta r_0 + \\
 & [-r_0(\lambda_r^- N_r^- - \lambda_r^+ N_r^+) + R_0 t_0 (W^- - W^+)] \delta R_0 - \\
 & r_0 \sin\phi^-(N_r^- + \gamma_{lm}) \delta z_0 + [(\cos\phi N_r + \gamma_{ms}) r]_{\infty} \delta r(\infty) = 0,
 \end{aligned} \tag{17}$$

where $z_0 = z(R_0)$. If the substrate is considered as rigid and flat, one has $\delta z_0 = 0$, $\phi^+ = \phi|_{\infty} = 0$, and $\phi^- = \phi_0$, which is defined as the elastic wetting contact angle, such that Eq. (17) can be simplified slightly,

$$\begin{aligned}
 & [\cos\phi_0(N_r^- + \gamma_{lm}) + (\gamma_{ls} - \gamma_{ms}) - N_r^+] r_0 \delta r_0 + \\
 & [-r_0(\lambda_r^- N_r^- - \lambda_r^+ N_r^+) + R_0 t_0 (W^- - W^+)] \delta R_0 + \\
 & [(N_r + \gamma_{ms}) r]_{\infty} \delta r(\infty) = 0.
 \end{aligned} \tag{18}$$

Besides, due to the axisymmetry, the membrane always satisfies

$$r(0) = z'(0) = 0. \tag{19}$$

Equation (18), including both elasticity and interface energy terms, gives rise to abundant boundary conditions at the contact line. We first consider an ultrasoft membrane sticking to the substrate (without slippage) through adhesion. In this context, we may neglect the elasticity terms in Eq. (18) and have $\delta r_0 \neq 0$, $\delta R_0 = 0$, $\delta r(\infty) = 0$. It is then natural to define the contact angle in this elasticity-free case as the effective Young's contact angle,

$$\cos\bar{\phi}_Y = \begin{cases} -1, & \beta \leq -1 \\ \beta, & \beta \in [-1, 1] \\ 1, & \beta \geq 1 \end{cases} \quad \text{where } \beta = \frac{\gamma_{ms} - \gamma_{ls}}{\gamma_{lm}}, \tag{20}$$

since it is analogous to Young's equation. With this definition, we may understand the essence of the contact line in the elastic wetting problem by examining how the elastic wetting contact angle ϕ_0 is evolved from the effective Young's contact angle $\bar{\phi}_Y$ when the elastic force acts on the contact line. The evolution would not only depend on the membrane properties but also vary with the extent to which the substrate constrains the membrane. We note that though $\bar{\phi}_Y$ is always within $[0, \pi]$, the term β is not limited to $[-1, 1]$. Physically,

$\beta \geq 1$ results in complete wetting whereas $\beta \leq -1$ corresponds to complete de-wetting at the interface. We will show that β is one of the two dimensionless groups that control the elastic wetting problem.

Though more subtleties would appear when the substrate is deformable (see discussion in Section 5.1), an understanding based on rigid substrates should be a starting point to grasp the physics and mechanics of elastic wetting. In particular, we consider four types of constraints on the contact lines as summarized in Table 2 and discussed in the following subsections, i.e. Sections 2.4.1-2.4.4.

2.4.1. Sliding boundary

We begin by discussing an imaginary contact line, the sliding boundary (see Column 2 of Table 2), where a membrane with an initial radius of R_0 is fixed vertically but free to slide laterally (i.e., not subjected to any horizontal constraints) at the contact line. The aim of considering this case of elastic wetting is to compare directly with a sessile drop (see Column 1 of Table 2). This comparison can be used to verify our theory by checking whether the elastic wetting degenerates to the classical wetting when membrane tension is trivial. More importantly, the comparison would provide simple, illustrative demonstrations of how the nonlinear elasticity modifies the classical Young's equation regarding the contact angle as well as the Young-Laplace equation regarding the normal force balance for a sessile drop. Based on the mechanism elucidated here, the results of more realistic boundary conditions will be presented in later sections.

Now, the $R > R_0$ part of the membrane is removed. The terms in Eq. (18) involving R_0^+ are set to be zero. In addition, the parameters defined in Eq. (20) need to be modified slightly by substituting γ_{ms} with γ_s , i.e.,

$$\beta = \cos \bar{\phi}_\gamma = \frac{\gamma_s - \gamma_{ls}}{\gamma_{lm}}. \quad (21)$$

The edge of the membrane could slide freely along the lateral direction, which means

$$\delta r_0 \neq 0, \delta R_0 = 0, \delta r(\infty) = 0. \quad (22)$$

Eq. (18) then becomes

$$[\cos \phi_0 (N_r^- + \gamma_{lm}) + (\gamma_{ls} - \gamma_s)] r_0 \delta r_0 = 0. \quad (23)$$

Eqs. (19) and (23) complete the boundary conditions required for solving the equilibrium Eq. (11) with a sliding boundary, namely

$$r(0) = z(R_0) = z'(0) = 0, \cos \phi_0 = \frac{\gamma_s - \gamma_{ls}}{N_r^- + \gamma_{lm}}. \quad (24)$$

Eq. (24) clearly suggests that the elastic wetting contact angle is a simple modification of the effective contact angle due to the membrane tension N_r^- at the contact line. Since the membrane tension term in Eq. (24) would be normalized by the in-plane stiffness, two dimensionless groups arise naturally; they are β (or $\bar{\phi}_\gamma$) in Eq. (21) and

$$\alpha = \frac{\gamma_{lm}}{\mu t_0}, \quad (25)$$

which compares the liquid-membrane interface energy density with the membrane stiffness and may be thought of as the *elasto-capillary* number in the elastic wetting problem. Systems with larger α are more likely to be dominated by their interface properties, otherwise by their membrane properties. Typical values of α are provided in Table 1, indicating that blisters with ultrathin and ultra-compliant biological membranes are more sensitive to the elasto-capillary effects.

2.4.2. Clamped boundary

In reality, there often exists a constraint on the membrane at the contact line due to either membrane-substrate adhesion or externally applied fixture. When the constraint is much stronger than the membrane and interfacial tension, it can be modeled as the clamped boundary that has been frequently used in classical bulge tests. Under this condition, the horizontal constraint could be treated as infinite, and the edge of the membrane is fixed on the rigid substrate (see Column 3 of Table 2), leading to

$$\delta r_0 = \delta R_0 = \delta r(\infty) = 0. \quad (26)$$

As a result, Eq. (18) is automatically satisfied. Eqs. (19) and (26) present the boundary conditions for equilibrium Eq. (11) with clamped boundary, namely

$$r(0) = z'(0) = z(R_0) = 0, r(R_0) = R_0. \quad (27)$$

In this case, only one controlling parameter appears in the normal equilibrium of Eq. (11), that is, the elasto-capillary number α .

2.4.3. Adhesive boundary

Instead of being infinite, the constraint along the contact line is usually limited by the adhesion between the membrane and the substrate. This is particularly true for liquid trapped between an adhesive interface aggregates into a blister (e.g., blisters formed when 2D crystals transferred on a substrate as shown in Fig. 1d) or when interfacial liquid generates and initiates membrane-substrate delamination (e.g., blisters form on hydrogel surface as shown in Fig. 1c). Either case shall be in equilibrium, although the

limitation of the horizontal constraint comes from work of adhesion in the former and work of separation in the latter. We study this equilibrium using an adhesive boundary (see Column 4 of Table 2), assuming Mode 2 delamination (tangential displacement at the contact line) negligible. For an equilibrated membrane-confined droplet (i.e., membrane-substrate delamination has propagated), we have $r_0 = R_0$ but R_0 is allowed to vary to minimize the total free energy or to achieve equilibrium. We therefore have

$$\delta r_0 = \delta R_0 \neq 0, \delta r(\infty) = 0. \tag{28}$$

As the tangential displacement at the contact line is not allowed, trivial solutions can be obtained for the attached membrane ($R \geq R_0^+$). The terms in Eq. (18) involving R_0^+ go to zero. With Eq. (28), Eq. (18) could be rewritten as

$$[\cos\phi_0(N_r^- + \gamma_{lm}) + (\gamma_{ls} - \gamma_{ms}) - \lambda_r^- N_r^- + t_0 W^-] r_0 \delta r_0 = 0. \tag{29}$$

Eqs. (19) and (29) then give rise to the boundary conditions for equilibrium Eq. (11) with adhesive boundary, namely

$$r(0) = z'(0) = z(R_0) = 0, \cos\phi_0 = \frac{\gamma_{ms} - \gamma_{ls} + \lambda_r^- N_r^- - t_0 W^-}{N_r^- + \gamma_{lm}}. \tag{30}$$

Like the case with the sliding boundary, this problem would depend on two dimensionless groups: α and β . The difference is that the β used for the adhesive boundary is defined by Eq. (20) while the β for the sliding boundary is defined by Eq. (21).

2.4.4. Slippery boundary

Finally, we consider an equilibrated droplet confined under an elastic membrane, where the membrane is allowed to slide laterally without shear resistance, which we call the slippery boundary (see Column 5 of Table 2). This boundary condition is motivated by two specific examples – 2D materials that feature an atomically smooth interface (Dai et al., 2018) or wet interfaces with negligible friction (Chopin et al., 2008). The bonded part is still considered as “attached” after horizontal slippage such that the interface energy remains unchanged. We will show that the “attached” membrane, in this case, is subjected to hoop compression due to the edge slippage, which is the differentiation from the sliding boundary. A more appropriate treatment is to release such compression via elastic instabilities. It warrants further investigations but is out of the focus of this work. Due to the slippage, we have $r_0 \neq R_0$ and both of them are unknown, i.e.,

$$\delta r_0, \delta R_0 \neq 0. \tag{31}$$

For the attached part ($R \geq R_0^+$), we have

$$r(R_0^+) = r_0, N_r|_{\infty} = -\gamma_{ms}, \tag{32}$$

as the boundary conditions for equilibrium Eq. (12). In computations, since the slippage at far-field is very trivial, we adopted a fixed displacement condition at the outer edge of the membrane, say $r(100R_0) = 100R_0$, for simplicity. Now Eq. (18) gives two conditions at the contact line,

$$\cos\phi_0 = \frac{\gamma_{ms} - \gamma_{ls} + N_r^+}{N_r^- + \gamma_{lm}}, \tag{33}$$

and

$$N_r^- \lambda_r^- - N_r^+ \lambda_r^+ = \frac{t_0 R_0 (W^- - W^+)}{r_0}. \tag{34}$$

Eqs. (33) and (34) can be used to solve for r_0 and R_0 , with boundary conditions for Eq. (11),

$$r(0) = z'(0) = 0, r(R_0^-) = r_0, z(R_0^-) = 0. \tag{35}$$

This case still relies on α and β .

Based on the equilibrium equations and boundary conditions given above, we adopted the well-established shooting method to solve the elastic wetting problem (such as the ODE45 solver in Matlab), which is presented in detail in Appendix B. In calculations, we used all normalized parameters (see details in Appendix B). The central deflection is normalized by r_0 as $z(0)/r_0$ to present the aspect ratio of the deformed blister. The volume is normalized as V/V_0 where $V_0 = \frac{4}{3}\pi R_0^3$. The inner pressure Δp is normalized to be $\Delta p R_0 / \mu t_0$ according to Eq. (B.5) or (B.6). Note that the normalized volume is a measure of the deformation of the thin membrane: a larger normalized volume suggests a larger deformation in the membrane. Besides, particular attention should be paid to adhesive and slippery boundaries because R_0 develops as the delamination propagates. We thus let the notation R_0 be the radius of the pre-existing delaminated zone and R_1 be the radius of the delaminated zone after interfacial delamination ($R_1 \geq R_0$) in the undeformed configuration (similarly, r_0 and r_1 in the deformed configuration).

3. Comparison between elastic wetting and classical wetting

In this section, we present numerical results for the elastic wetting problem with the imaginary sliding boundary (Column 2 of

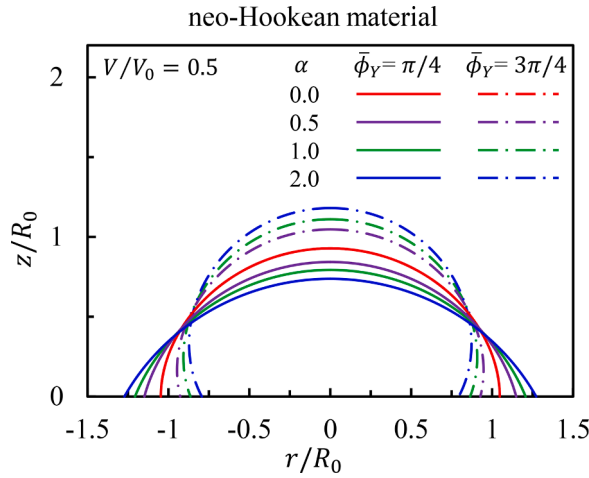


Fig. 3. Profiles of droplets confined by neo-Hookean membranes subjected to sliding boundary conditions. $V/V_0 = 0.5$ is prescribed while the elasto-capillary numbers α is varying. Solid curves correspond to $\bar{\phi}_Y = \pi/4$ and dash-dot curves for $\bar{\phi}_Y = 3\pi/4$. The two red curves overlay.

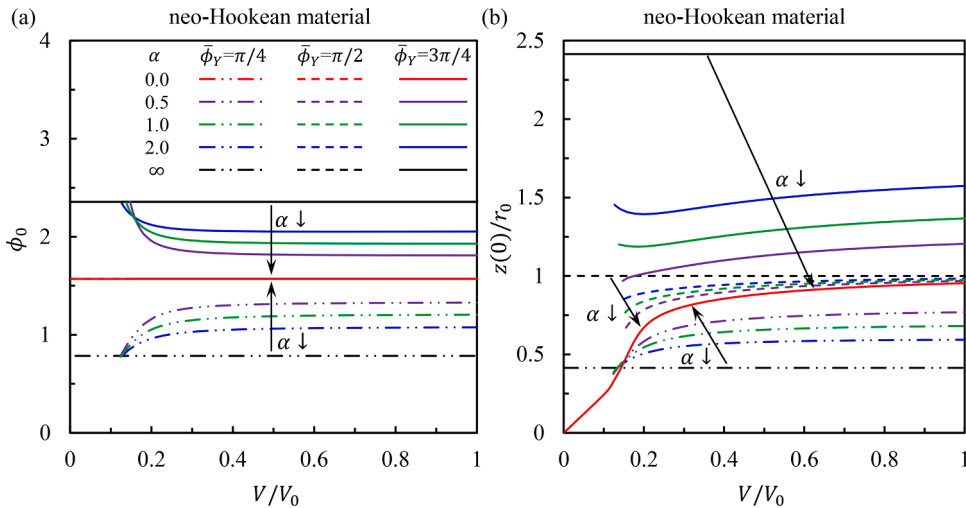
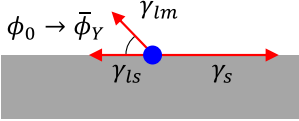
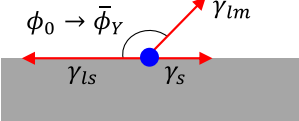
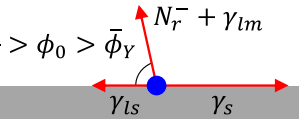
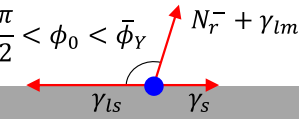
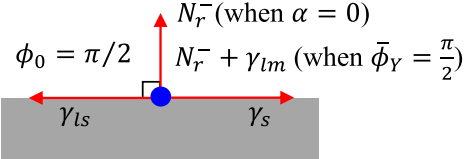


Fig. 4. The evolution of (a) the elastic wetting contact angle and (b) the aspect ratio of droplets confined by neo-Hookean membranes subjected to sliding boundary conditions for $\bar{\phi}_Y = \pi/4$ (dash-dot-dot curves), $\pi/2$ (dashed curves) and $3\pi/4$ (solid curves) with various α . The arrows indicate α decreases from ∞ to 0 . In (a), all the dashed curves and red curves (i.e., when $\bar{\phi}_Y = \pi/2$ or $\alpha = 0$) collapse to the red solid line. In (b), all the red curves (i.e., when $\alpha = 0$) collapse to the red solid curve.

Table 2), which could be understood via several concepts in the classical wetting problem. As a demonstration, in Fig. 3, we first show profiles of membrane-confined droplets with a hydrophilic and a hydrophobic effective Young’s contact angle $\bar{\phi}_Y$, $\pi/4$ (solid curves) and $3\pi/4$ (dash-dot curves), respectively, under a prescribed volume of $V/V_0 = 0.5$ for various elasto-capillary numbers α . When $\alpha = 0$, the profiles of these blisters, i.e. the two overlapping red curves, are controlled by the elasticity of the membrane, featuring an elastic wetting contact angle of $\pi/2$ regardless of the effective Young’s contact angle. As α increases, the elastic wetting contact angle starts to deviate from $\pi/2$ due to the effect of interfacial tension, till it approaches $\bar{\phi}_Y$.

We further plot the evolution of the elastic wetting contact angle ϕ_0 and the aspect ratio $z(0)/r_0$ vs. V/V_0 under various effective Young’s contact angle $\bar{\phi}_Y$ and elasto-capillary number α in Fig. 4. As expected, $\phi_0 \rightarrow \bar{\phi}_Y$ as $\alpha \rightarrow \infty$ regardless of the deformation as represented by the three horizontal lines in Fig. 4a. This result confirms that elastic wetting with a sliding boundary (Column 2 of Table 2) could indeed decay to classical wetting (Column 1 of Table 2) when the interfacial tension dominates over the membrane elasticity, i.e., $\gamma_{lm} \gg N_r^-$. Since the sessile drop in classical wetting exhibits a spherical cap shape, the aspect ratio should remain constant at a given $\bar{\phi}_Y$ regardless of the liquid volume, which is consistent with our numerical solutions when $\alpha \rightarrow \infty$ (see the three horizontal lines in Fig. 4b). In contrast, when the elastic force dominates, i.e. $\alpha \rightarrow 0$, all curves consolidate into the red horizontal line in Fig. 4a, i.e. $\phi_0 \equiv \pi/2$, indicating that all cases decay to the case of air bulging of a thin membrane (i.e., $\alpha = 0$). Therefore, the corresponding aspect ratio-deformation relations are independent of $\bar{\phi}_Y$, i.e., all the red curves in Fig. 4b collapse to the solid red curve. Also obvious in Fig. 4b, only when the deformation is relatively large (i.e., $V/V_0 \geq 0.8$ so that elasticity dominates), the blisters with α

Table 3
Illustrations of force balance at the contact line (blue dots) in elastic wetting with sliding boundaries.

	$\bar{\phi}_Y < \frac{\pi}{2}$	$\bar{\phi}_Y > \frac{\pi}{2}$
Small deformation $\gamma_{lm} \sim (\gamma_s - \gamma_{ls}) \gg N_r^-$	 $\gamma_{lm} \sim \gamma_s \gtrsim \gamma_{ls} \gg N_r^-$	 $\gamma_{lm} \sim \gamma_{ls} \gtrsim \gamma_s \gg N_r^-$
Large deformation $\gamma_{lm} \sim (\gamma_s - \gamma_{ls}) \sim N_r^-$	 $N_r^- \sim \gamma_{lm} \sim \gamma_s \gtrsim \gamma_{ls}$	 $N_r^- \sim \gamma_{lm} \sim \gamma_{ls} \gtrsim \gamma_s$
$\bar{\phi}_Y = \pi/2$ or $\alpha = 0$	 $\gamma_s = \gamma_{ls}$	

= 0 could approach a hemispherical profile (i.e., aspect ratio approaching 1). In more general cases, when $\bar{\phi}_Y \neq \pi/2$ and α is nonzero and finite, the elastic wetting contact angle ϕ_0 should be determined by both interfacial and elastic tensions and the latter could be tuned by the deformation of the thin membrane (see Fig. 4).

The elastic wetting contact angle is sensitive to the droplet volume when $V/V_0 < 0.4$, i.e. when elasticity cannot fully dominate over interfacial tension (see Fig. 4a). This could be understood through the investigation of how the elasticity (favoring $\pi/2$) modifies the Young’s equation (favoring $\bar{\phi}_Y$), which is further illustrated by the force balance at the contact line in Table 3. We will focus our discussion on the case of $\bar{\phi}_Y < \pi/2$ but the physical argument also applies to the case of $\bar{\phi}_Y > \pi/2$. In this context, though numerical solution allows $\phi_0 < \bar{\phi}_Y$, we found that the stretches at the center of the membrane are only greater than 1 (i.e. the membrane is in tension) when $\phi_0 > \bar{\phi}_Y$. Therefore, we focus on numerical results in Fig. 4a with $\phi_0 \in (\bar{\phi}_Y, \pi/2)$. As a result, the corresponding aspect ratio-deformation curves in Fig. 4b do not emanate from the origin when α is nonzero and finite. Specifically, for systems with $\phi_0 \sim \bar{\phi}_Y$, the membrane tension is relatively small ($\lambda_r, \lambda_\theta \sim 1$), hence the tangential force is dominated by the liquid/membrane interfacial tension γ_{lm} (see the 1st row of Table 3). As the deformation increases, the membrane tension provides a modification to the classical Young’s equation (see Eq. (24)) or an additional force that lifts the $\bar{\phi}_Y$ towards $\pi/2$ (see the 2nd row of Table 3). This process is best illustrated by an animation of a numerically solved blister profile evolution with a sliding boundary in supplementary Video 1. For the specific cases of either $\bar{\phi}_Y = \pi/2$ or $\alpha = 0$, both the membrane tension and the liquid/membrane interfacial tension at the contact line are vertical, which satisfies the horizontal “force equilibrium” (see the 3rd row of Table 3). As a result, the elastic wetting contact angle remains to be $\pi/2$ and all the dashed and red curves in Fig. 4a collapse to the red solid line. However, the dashed curves do not collapse in Fig. 4b as those in Fig. 4a. This is because the interfacial tension exerted at the contact line increases as α increases, which lifts the aspect ratio.

Besides the blister profiles, the inner blister pressure is another important parameter, particularly for 2D-material-confined liquids with possible applications such as interface-confined high-pressure (e.g. 2 GPa) chemistry (Lim et al., 2014). We hence plot the normalized pressure vs. deformation in Fig. 5. Since the normal equilibrium is a simple summation of the membrane-tension induced pressure and the Young-Laplace pressure as given in the first equation of Eq. (11), a system with a larger elasto-capillary number would produce larger Young-Laplace pressure under the same level of deformation. Note that at large deformations, the nonlinear elasticity of the membrane could release the pressure, reminiscent of the snap-through instability while inflating a neo-Hookean balloon. The

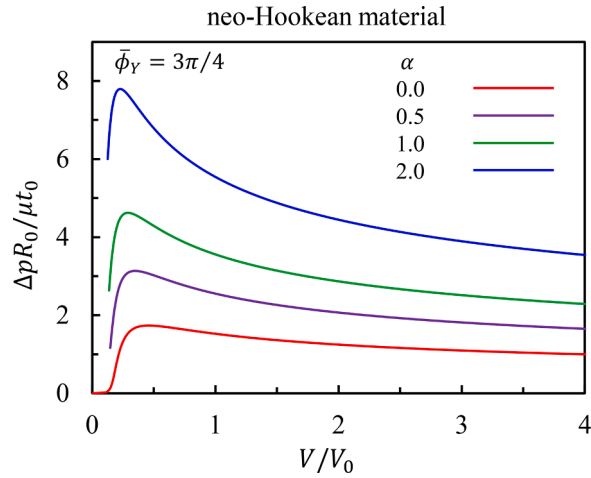


Fig. 5. Normalized pressure-deformation relations for elastic wetting with neo-Hookean membranes and sliding boundaries under various elasto-capillary numbers α .

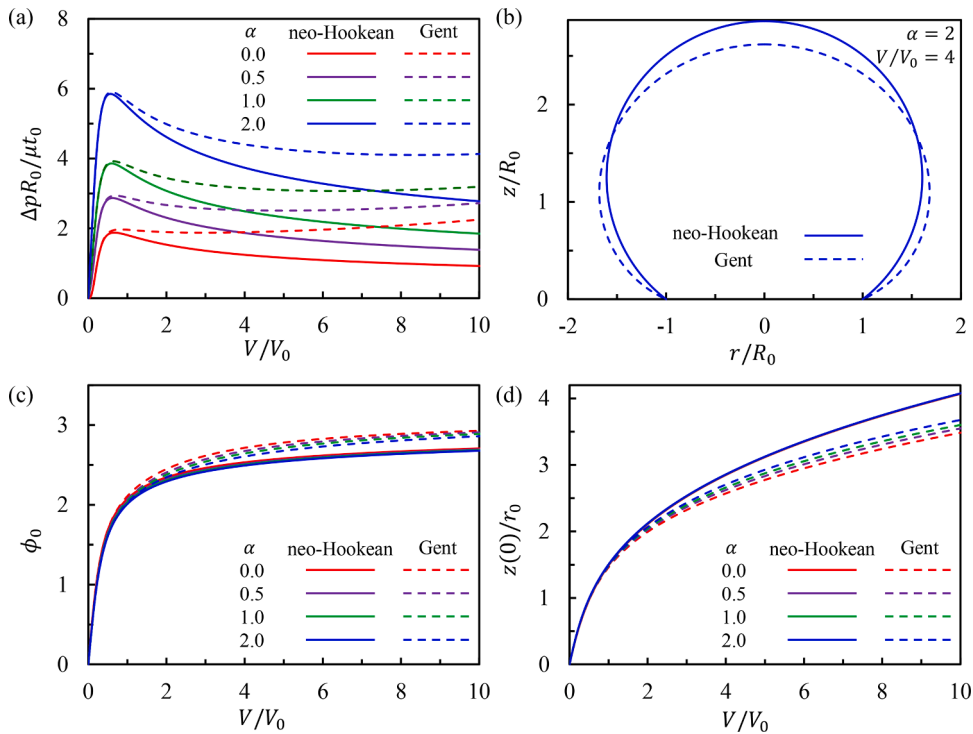


Fig. 6. Solutions to elastic wetting under clamped boundary with various elasto-capillary numbers α and different membrane constitutive laws – neo-Hookean (solid curves) vs. Gent (dashed curves). (a) Normalized pressure-deformation relation. (b) Blister profiles at given $\alpha = 2$ and $V/V_0 = 4$. (c) Elastic wetting contact angle-deformation relation. (d) Aspect ratio-deformation relation.

results in Figs. 3-5 are based on the neo-Hookean constitutive law. Results based on the Gent constitutive law only show slight quantitative differences and therefore are presented in –Figs. C1-C3 in Appendix C.

Our model and solution for the elastic wetting problem with a sliding boundary reveal the dramatically changed droplet profile and pressure from classical wetting, which is attributed to the elasticity-surface/interface tension interaction. Due to the limitations in accurately detecting the edge profiles at small scales, we realize that the aspect ratio (see Fig. 4b) may be a more practical geometric feature to measure in experiments, whereas the elastic wetting contact angle can be leveraged as a mathematical tool to elucidate the force balance at the contact line. Therefore, to unveil elastic wetting problems subjected to other contact/boundary conditions, in what follows, we present the numerical results in terms of the pressure, the profile, the elastic wetting contact angle, and the aspect ratio of the soft membrane-confined droplet.

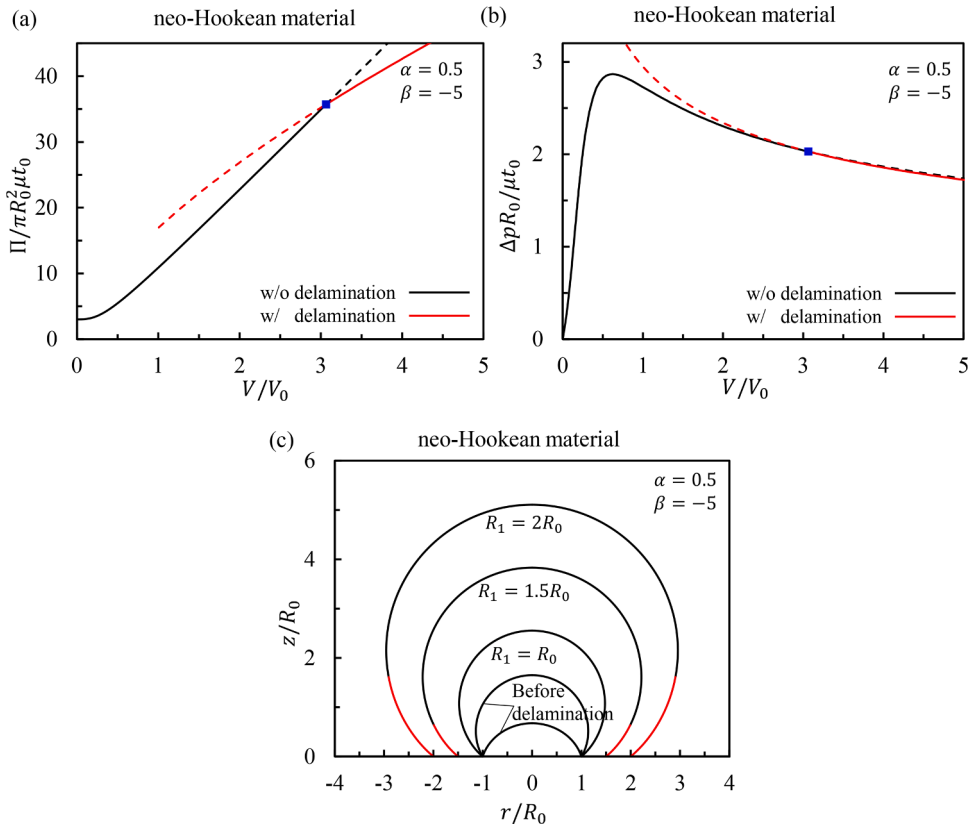


Fig. 7. Normalized (a) free energy-deformation and (b) pressure-deformation relations for elastic wetting with a neoHookean membrane and an adhesive boundary when $\alpha = 0.5$ and $\beta = -5$ are given. The black and red curves represent configurations without and with edge delamination, respectively. The solid curves represent the actual evolution pathways of free energy/pressure. The blue marker at the intersection of the black and red curves highlights the critical volume-to-delaminate. (c) The growth of the blister profile under the adhesive boundary. The black and red parts represent the sections of the membrane that are initially detached from or attached to the substrate before any liquid injection. In other words, the red parts are delaminated membrane due to the increased liquid volume. For the two blister profiles labeled with “before delamination”, their prescribed volumes are $V/V_0 = 0.3$ and 0.9 .

4. Solutions to elastic wetting under different boundary conditions

In this section, we consider elastic wetting with more realistic boundary conditions listed in Table 2. We first assign an infinite constraint, i.e. a clamped boundary (see Column 3 of Table 2). We then consider finite horizontal constraint due to the finite membrane-substrate adhesion, which leads to edge delamination without slippage (see Column 4 of Table 2) and with slippage (see Column 5 of Table 2). We note that there may exist an initially delaminated area in experiments (Benet and Vernerey, 2019; Shen et al., 2019). After the membrane is further inflated, the problem is first under clamped boundary and then subjected to edge delamination when the membrane tension is substantial enough to cause the membrane-substrate interface failure (Benet and Vernerey, 2019).

4.1. No edge delamination (clamped boundary)

Of interest is the process of the quasi-static inflation of liquids at the membrane-substrate interface (a.k.a. blistering or bulging) with pre-existing circular delamination of radius R_0 . Before further delamination occurs, the system can be considered as elastic wetting with a clamped boundary, as illustrated by Column 3 of Table 2. Classical bulging solutions considered material and geometric nonlinearity but not interfacial tension (Wang et al., 2017a; Xie et al., 2016). Taking interfacial tension into consideration, we numerically solve the boundary value problem defined in Section 2.4.2.

Fig. 6a plots the normalized pressure-deformation relation of different α based on two different material laws. Similar to the sliding boundary discussed in Section 3, a higher elasto-capillary number yields higher pressure. Unlike the sliding boundary, the clamped boundary shows a discernable deviation between the two material laws at large deformations (i.e., $V/V_0 > 1$). Specifically, as the liquid volume increases, the pressure first increases dramatically and then decreases gradually for a neo-Hookean membrane, whereas an N-shaped pressure-deformation curve is observed for a Gent membrane. The difference is attributed to the strengthening phenomena included in the Gent model when the applied stretch approaches the limiting stretch of the polymer chains, i.e., $I_1 - 3 \rightarrow J_m$ ($J_m = 100$ in our computation). Consequently, given the same volume, the droplet confined by a Gent membrane is predicted to exhibit

smaller aspect ratios than that under a neo-Hookean membrane of the same shear modulus (see Fig. 6b). In fact, with the clamped boundary, both the elastic wetting contact angle and the aspect ratio can be tuned by the liquid volume, as shown in Figs. 6c and 6d. It is worth noting that the elastic wetting contact angle and the aspect ratio of the droplet confined by neo-Hookean membranes are insensitive to the elasto-capillary number α whereas the Gent membrane leads to slightly decreasing elastic wetting contact angle and increasing aspect ratio with increasing α , especially at large deformation. We again attribute such difference to the strengthening effect of the Gent model at large deformation. The quasi-static growth process of a droplet confined by a neo-Hookean membrane with a clamped boundary can be visualized through supplementary Video 2.

4.2. Edge delamination without slippage (adhesive boundary)

4.2.1. Solutions to edge delamination without slippage

The assumption of clamped boundary breaks down when edge delamination occurs as the base radius of the blister starts to vary. We first consider an adhesive boundary that allows normal separation but prohibits horizontal slippage at the membrane-substrate interface. Hence the undelaminated part of the membrane is stress-free. The criterion of edge delamination is that the elastic wetting contact angle satisfies the boundary conditions expressed in Eq. (30) (also included in Column 4 of Table 2). As we discussed in Section 2.4.3, this criterion depends on two dimensionless groups: α (i.e., $\gamma_{lm}/\mu t_0$) and β (i.e., $(\gamma_{ms} - \gamma_{ls})/\gamma_{lm}$). The numerical solutions to the adhesive boundary are plotted in Figs. 7 through 9. The critical volume-to-delaminate can be determined through the comparison of the total free energy of undelaminated (black) and delaminated (red) configurations, as plotted in Fig. 7a, where $\alpha = 0.5$ and $\beta = -5$. The intersection is marked by a blue square, where the criterion is first satisfied or beyond which edge delamination occurs. Fig. 7b plots the normalized inner pressure before (black) and after (red) edge delamination. Hence the actual pressure should evolve along the black curve at small volumes and then along the red curve beyond the blue marker, i.e. along the solid curves in Fig. 7b.

Red curves in Fig. 7 are obtained by considering that the edge of the blister has delaminated to enlarge the radius from r_0 (or R_0 in the undeformed configuration) to r_1 (or R_1 in the undeformed configuration), where $r_0 = R_0$ and $r_1 = R_1$ due to prohibited edge slippage and $R_1 \geq R_0$. To calculate the pressure and profile of the delaminated blister, we may consider the elastic wetting problem with a clamped boundary but using parameters V/V_1 (where $V_1 = 4\pi R_1^3/3$), $\Delta p R_1/\mu t_0$, z/r_1 and ϕ , all normalized based on R_1 . The advantage of this normalization is that the critical pressure or volume relies only on α and β and is independent of any lengths, including the radius of the pre-existing delamination zone. In other words, $(V/V_1)_c = (V/V_0)_c$ and $(\Delta p R_1/\mu t_0)_c = (\Delta p R_0/\mu t_0)_c$ for any $R_1 \geq R_0$. However, it is still convenient to plot the delaminated pressure-deformation relation by the coordinates based on R_0 (e.g., $\Delta p R_0/\mu t_0$ and V/V_0). We hence leverage the following relation to cancel out the radius R_1 :

$$V \left(\frac{\Delta p}{\mu t_0} \right)^3 = C(\alpha, \beta). \tag{36}$$

Eq. (36) gives rise to the red curve in Fig. 7b, where the constant $C(\alpha, \beta)$ is determined by the fact that Eq. (36) has to pass the blue marker (i.e., the critical delamination point). As long as this criterion is satisfied, the pressure-deformation curve would switch from the black to the red curve that denotes equilibrated states. Similar relations for Gent membranes are shown in Fig. C4 in Appendix C, where we find that the edge delamination initiates earlier than the droplet confined by the neo-Hookean membrane due to the strengthening effect of the Gent membrane.

The profiles of the blister before and after delamination are plotted in Fig. 7c. Before edge delamination, i.e. $V/V_0 < (V/V_0)_c$, the membrane-confined droplet behaves like a clamped blister and we plot two of them with prescribed volumes of $V/V_0 = 0.3$ and 0.9 as labeled in Fig. 7c. Once $V/V_0 \geq (V/V_0)_c$, edge delamination kicks in. The new system could be thought of as having a pre-existing delamination zone of radius R_1 . Its deformation level satisfies $V/V_1 = (V/V_1)_c$ and its normalized profile $z \left(\frac{r}{R_1} \right) / R_1$ is identical to the profile $z \left(\frac{r}{R_0} \right) / R_0$ at the critical moment defined by $V/V_0 = (V/V_0)_c$. In other words, by doing normalization, all numerical solutions for elastic wetting after edge delamination are identical to the numerical solution for elastic wetting at the critical moment. It is useful to plot the profile of a delaminated droplet with R_1 along with the normalization based on R_0 , which could be readily achieved by scaling the profile of the critical moment through $\frac{r}{R_0} \rightarrow \frac{R_1}{R_0} \frac{r}{R_0}$ and $\frac{z}{R_0} \rightarrow \frac{R_1}{R_0} \frac{z}{R_0}$. In Fig. 7c, it is clear that the profiles after delamination are self-similar as they were obtained by simply scaling the profile at the critical moment. Such volume-independent self-similarity has been widely found in 2D-material-confined droplets in the literature (Khestanova et al., 2016; Sanchez et al., 2018). The growing process of a neo-Hookean membrane confined droplet under the adhesive boundary is visualized through supplementary Video 3.

4.2.2. A means to determine (α, β) and membrane-substrate adhesion energy Γ

Since the solutions V/V_1 , $\Delta p R_1/\mu t_0$, $z(0)/r_1$ and ϕ_0 are only dependent on α and β in elastic wetting with adhesive boundary, we provide the contour plots for these dependencies in Fig. 8 for droplets under neo-Hookean membranes. Of particular interest is the discovery of the blank spaces in these contour plots, where numerical methods failed to find solutions. The left-side blank space features large α and small β . The physical interpretation is that the membrane-substrate adhesion is sufficiently strong to prevent interface delaminating no matter how much the volume inflates. We will show later in Eq. (38) that the membrane-substrate interface adhesion energy is related to $\alpha(1 - \beta)$. We note that the left-side blank space disappears in the contour plots for droplets confined by Gent membranes (see Fig. C5 in Appendix C), which suggests the interface could delaminate eventually due to the strengthening of the Gent membrane. The right-side blank space exists for both neo-Hookean and Gent membranes and could be captured simply by $\beta \geq 1$.

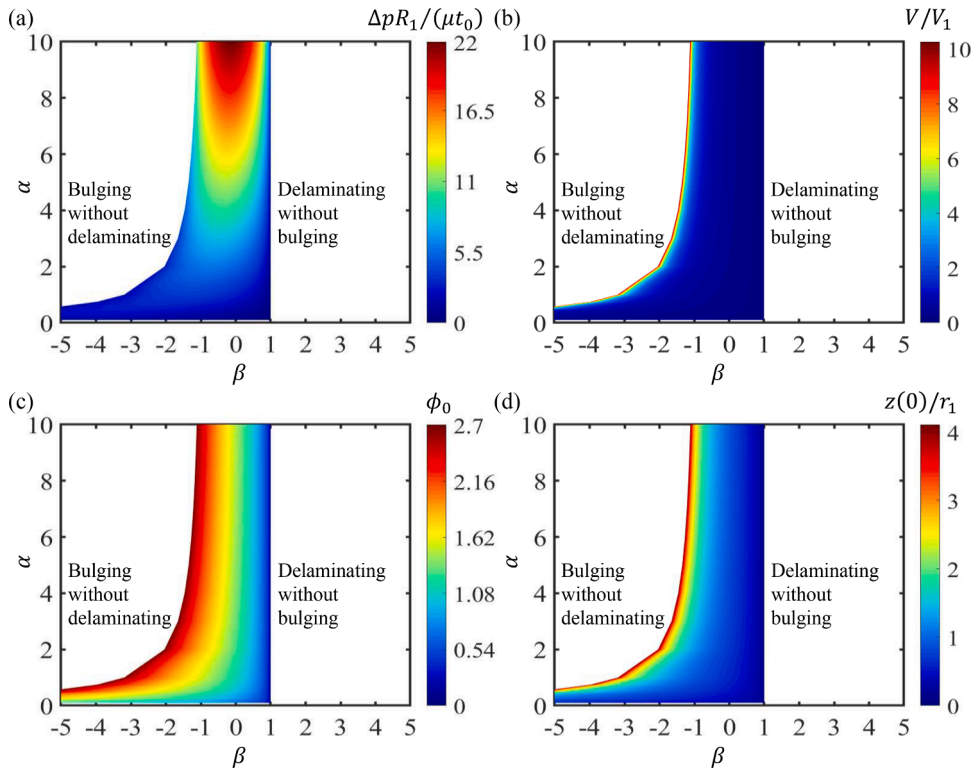


Fig. 8. Contour plots of (a) the normalized pressure, (b) the normalized volume, (c) the elastic wetting contact angle, and (d) the aspect ratio in $\alpha \sim \beta$ parametric space for elastic wetting with neo-Hookean membranes and adhesive boundaries.

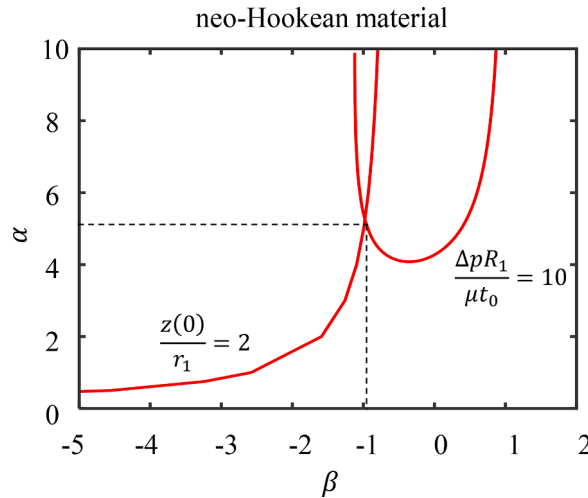


Fig. 9. Contour curves for $z(0)/r_1 = 2$ and $\Delta p R_1 / \mu t_0 = 10$ in $\alpha \sim \beta$ parametric space for elastic wetting with a neo-Hookean membrane and an adhesive boundary.

$= 1$ is equivalent to $\mathcal{S} = \gamma_{ms} - \gamma_{ls} - \gamma_{lm} = 0$, where \mathcal{S} is called the *elastic wetting spreading number*, reminiscent of the spreading number for classical wetting (Quéré et al., 1990). When $\mathcal{S} \geq 0$ or $\beta \geq 1$, the interface is in complete wetting ($\phi_0 = 0$) so that liquid spreads along the interface without bulging the membrane. This scenario has been observed in 2D material systems, where the membrane and the substrate are relatively hydrophilic, and the membrane-substrate adhesion is relatively weak (Temmen et al., 2014).

While the membrane elastic properties are relatively accessible, the interface energies are notoriously challenging to detect experimentally (Calvimontes, 2017). It hence gives rise to the challenge of determining the controlling parameter group (α, β) in elastic wetting problems. Our contour plots suggest that for a regular elastic wetting system with $\phi_0 \in (0, \pi)$, α and β could be extracted

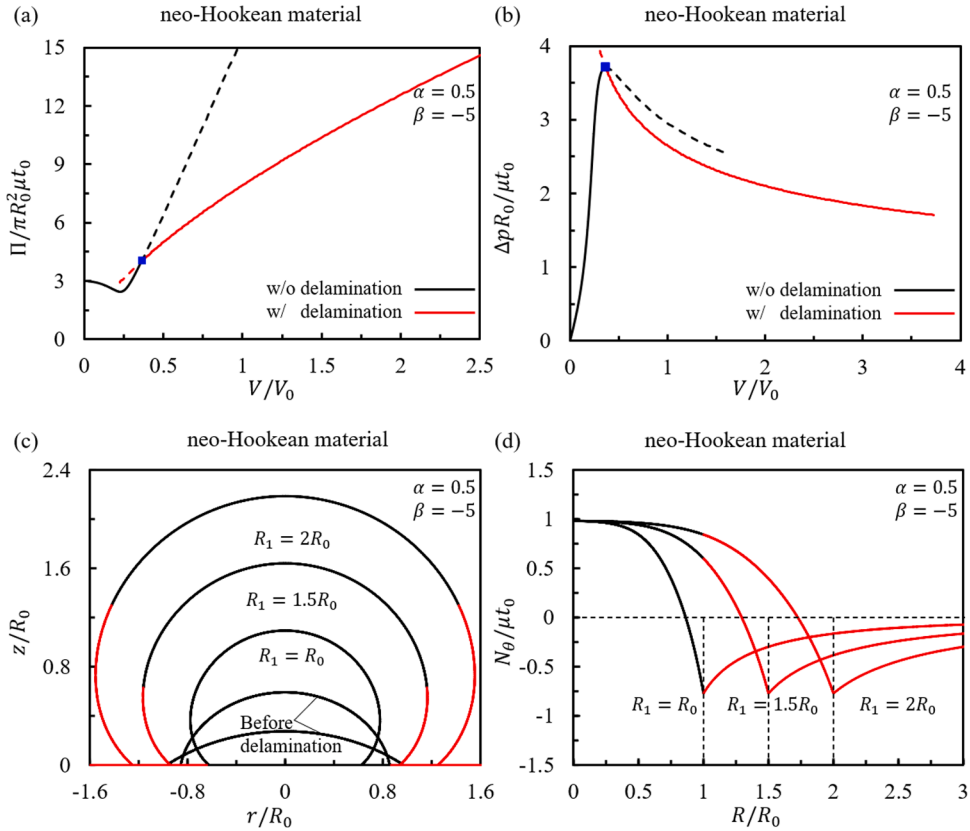


Fig. 10. Normalized (a) free energy-deformation and (b) pressure-deformation relations for elastic wetting with a neo-Hookean membrane and a slippery boundary when $\alpha = 0.5$ and $\beta = -5$ are given. The black and red curves represent configurations without and with edge delamination, respectively. (c) The growth of the blister profile under the slippery boundary. The black and red parts represent the sections of the membrane that are initially detached from or attached to the substrate before any liquid injection. For the two blister profiles before delamination, their prescribed volumes are $V/V_0 = 0.1$ and 0.2 . (d) Normalized hoop tension in the membrane with edge delamination of $R_1 = R_0, 1.5R_0$, and $2R_0$.

once the droplet pressure and one of the three geometrical parameters in Fig. 8 could be measured. It is theoretically possible to extract (α, β) purely through two of the three geometrical parameters, $V/V_1, z(0)/r_1$ and ϕ_0 . But the error could be excessive since these geometrical parameters share a very similar dependency on α and β (see Fig. 8). We thus advocate exploiting the combination of pressure and one of the geometrical parameters, such as the aspect ratio. For example, for a droplet covered by a neo-Hookean membrane with $z(0)/r_1 = 2$ and $\Delta p R_1 / \mu t_0 = 10$, one can plot corresponding contour curves using Figs. 8a and 8d, and the intersect yields the α and β of the system (Fig. 9). While the aspect ratio is often easy to detect in experiments, directly measuring the pressure in micro- or nano- blisters is almost impossible. We will propose an approach to estimate the pressure in Section 5.1 by observing the substrate deformation if the substrate were not completely rigid. The same methodology could be adopted to find out (α, β) for droplets confined by Gent membranes (see Fig. C6 in Appendix C).

Knowing α and β of the elastic wetting system with adhesive boundary can shed light on the membrane-substrate adhesion energy Γ . Specifically, according to the definition,

$$\Gamma = \gamma_s + \gamma_m - \gamma_{ms}, \tag{37}$$

where γ_s and γ_m are the surface energy densities of the substrate and the membrane, respectively. We may apply Young's equation such that Eq. (37) yields

$$\frac{\Gamma}{\mu t_0} = \alpha(1 - \beta) + \frac{\gamma_l}{\mu t_0} (\cos \phi_m + \cos \phi_s), \tag{38}$$

where γ_l is the surface tension of the interfacial liquid, and ϕ_m and ϕ_s are Young's contact angles of the interfacial liquid on the membrane and the substrate, respectively. Therefore, the membrane-substrate adhesion energy can be estimated once the membrane stiffness (i.e., μt_0) and surface parameters (including $\alpha, \beta, \gamma_l, \phi_m$, and ϕ_s) in the system are known. The extracted Γ could be either work of adhesion or work of separation, depending on whether the droplet is formed via a process of the membrane healing with or separating from the substrate.

4.3. Edge delamination with slippage (slippery boundary)

Finally, we allow the membrane to delaminate with free slippage against the substrate so that the membrane in contact with the substrate is stressed. The main difference between edge delamination without and with slippage is that $r_1 \neq R_1$ in the later. The criteria for delamination with slippage should include the force balance at the contact, i.e. Eq. (33), plus an equation, i.e. Eq. (34), to relate r_1 to R_1 . The physical concepts discussed in Section 4.2.1 such as the self-similar shape and the invariant $V \left(\frac{\Delta p}{\mu t_0} \right)^3$ are still applicable to this case.

We plot the normalized free energy-deformation and normalized pressure-deformation relations before and after edge delamination in Figs. 10a and 10b, respectively. The blue marker locates the onset of delamination when $\alpha = 0.5$ and $\beta = -5$ are given. Compared to the position of the blue marker shown in Fig. 7a or Fig. 7b, at the same α and β , the edge delamination occurs much earlier in a membrane-confined droplet with slippery boundary because the membrane-substrate interface is relatively weak compared with the adhesive boundary. Fig. 10c plots the evolution of the blister profile. After the onset of delamination, the profiles are again obtained through scaling the profile at the onset of delamination. Notably, the radius of the contact line first shrinks at the early stage of the bulging, reminiscent of the experimental observation of a flat membrane suddenly wrapped around a droplet due to surface tension (Antkowiak et al., 2011; de Langre et al., 2010; Paulsen et al., 2015). The wrapping and delamination process under slippery boundary can be visualized in supplementary Video 4. Figure 10d exhibits the distribution of normalized hoop tractions in the membrane with edge delamination $R_1 = R_0, 1.5R_0$, and $2R_0$. It is clear that all the attached region and part of the bulged region of the membrane are subjected to hoop compression. Considerations of elastic instabilities that release such compression would be necessary (Chopin et al., 2008; Dai and Lu, 2021; Dai et al., 2020b; Huang et al., 2007), but are out of the scope of this paper. Besides, similar results for elastic wetting with a Gent membrane and a slippery boundary are offered in Fig. C7 in Appendix C.

We have provided the full theoretical solutions to elastic wetting under three realistic boundary conditions in this section. We find that before edge delamination occurs, the system with adhesive boundary first behaves like a clamped bulge test where the interfacial tension and the membrane tension together balance against the inner pressure through curvature, while the contact line of the system with slippery boundary first moves inward such that the membrane appears to wrap around the interfacial droplet. Once the bulging volume reaches the critical volume-to-delaminate or the contact angle reaches the critical value as given in Eq. (30) for non-slipping interface and Eq. (33) for slipping interface, edge delamination occurs, and the blister grows in a self-similar manner with constant contact angle afterward. Everything else the same, the slippery boundary greatly reduces the critical volume-to-delaminate compared with the adhesive boundary due to a weaker membrane-substrate interface. Once the membrane slides inward under slippery boundary, hoop compression develops in the membrane, which would cause instabilities such as radial buckles but is beyond the scope of this work.

5. Discussions

5.1. Effects of substrate compliance

Having shown the complexities in pressure and geometry when the droplet is confined between an elastic membrane and a rigid substrate, we discuss the applicability of our theory when the substrate is not perfectly rigid.

To reveal the effects of substrate stiffness, we start with a simple scaling analysis for the elastic wetting problem on a soft substrate subjected to a clamped boundary. Based on equilibrium Eq. (11), the inner pressure can be expressed as $\Delta p \sim (N + \gamma)\kappa$. Consider the membrane strain $\varepsilon \sim (h/R_0)^2$, the membrane tension $N \sim \mu t_0 \varepsilon \sim \mu t_0 (h/R_0)^2$ and the curvature $\kappa \sim h/R_0^2$, we have $\Delta p \sim \mu t_0 h^3 / R_0^4 + \gamma h / R_0^2$. Furthermore, the central deflection of the substrate, i.e. δ_s , due to the inner pressure is less than $\Delta p R_0 / \mu_s \sim \frac{\mu t_0}{\mu_s} (h^3 / R_0^3 + \alpha h / R_0)$ (Lubarda, 2013). Consequently, the ratio of the central deflection of the substrate to the central deflection of the membrane can be expressed as $\delta_s / h < \sim \frac{\mu t_0}{\mu_s R_0} (h^2 / R_0^2 + \alpha)$. In most experiments, $h/R_0 \sim \mathcal{O}(1)$ and $\alpha < \sim 1$ (see the 3rd and the 7th rows of Table 1). Therefore, we suggest that the effect of substrate compliance on the droplet configuration may be negligible when $\mu t_0 / (\mu_s R_0) \ll 1$. Considering the fact that t_0/R_0 is extremely small for ultrathin membrane systems, our theoretical analysis based on the rigid substrate would stay applicable as long as the membrane stiffness is not orders of magnitude larger than that of the substrate. This also brings an outstanding opportunity to detect the elusive inner pressure of membrane-confined droplets via the substrate deformation (Latorre et al., 2018), which should be sufficiently large to allow for accurate experimental measurement yet sufficiently small (compared with the membrane deflection) to render our rigid substrate assumption valid. Such a conclusion essentially makes use of the nearly linear elasticity of an elastomeric substrate at small deformation and the highly nonlinear elasticity of a thin membrane at large deformation.

We quantitatively verify the rigid substrate criterion of $\mu t_0 / (\mu_s R_0) \ll 1$ by carrying out finite element modeling (FEM) in Abaqus. The elasto-capillary effect is simulated by using the UEL subroutine created by Jagota and colleagues (Jagota et al., 1998; Style et al., 2017; Xu et al., 2014), where a two-node user-defined surface element was developed and applied in various topics involving surface tensions. In our simulations, both the thin membrane and the substrate were modeled as incompressible neo-Hookean materials. The substrate was meshed using 2-D axisymmetric elements CAX4H. We chose a domain $\Omega = \{(R, Z) | 0 \leq R \leq 10R_0, -10R_0 \leq Z \leq 0\}$ whose lateral size and depth were both ten times of the initial blister radius, i.e. $10R_0$, such that the substrate could be treated as a half-space. We considered small substrate-liquid and substrate-membrane interface energies and large membrane-liquid interface energies such that the substrate was susceptible to deformation under a given blister height. Specifically, $\gamma_{ls} = \gamma_{ms} = 0$ and $\gamma_{lm} / \mu t_0 = 1$

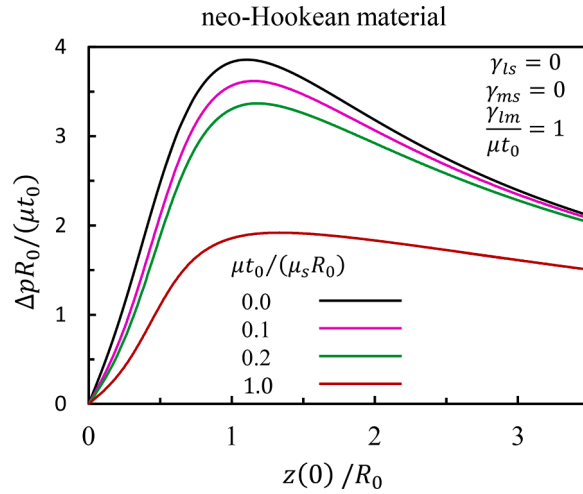


Fig. 11. FEM results of the normalized pressure against the normalized central displacement of the neo-Hookean membrane with a clamped boundary on soft substrates where $\mu t_0/(\mu_s R_0) = 0, 0.1, 0.2, 1.0$, $\gamma_{ls} = \gamma_{ms} = 0$ and $\gamma_{lm}/\mu t_0 = 1$. The result of $\mu t_0/(\mu_s R_0) = 0$ (the black curve) represents the elastic wetting with a clamped boundary on a rigid substrate.

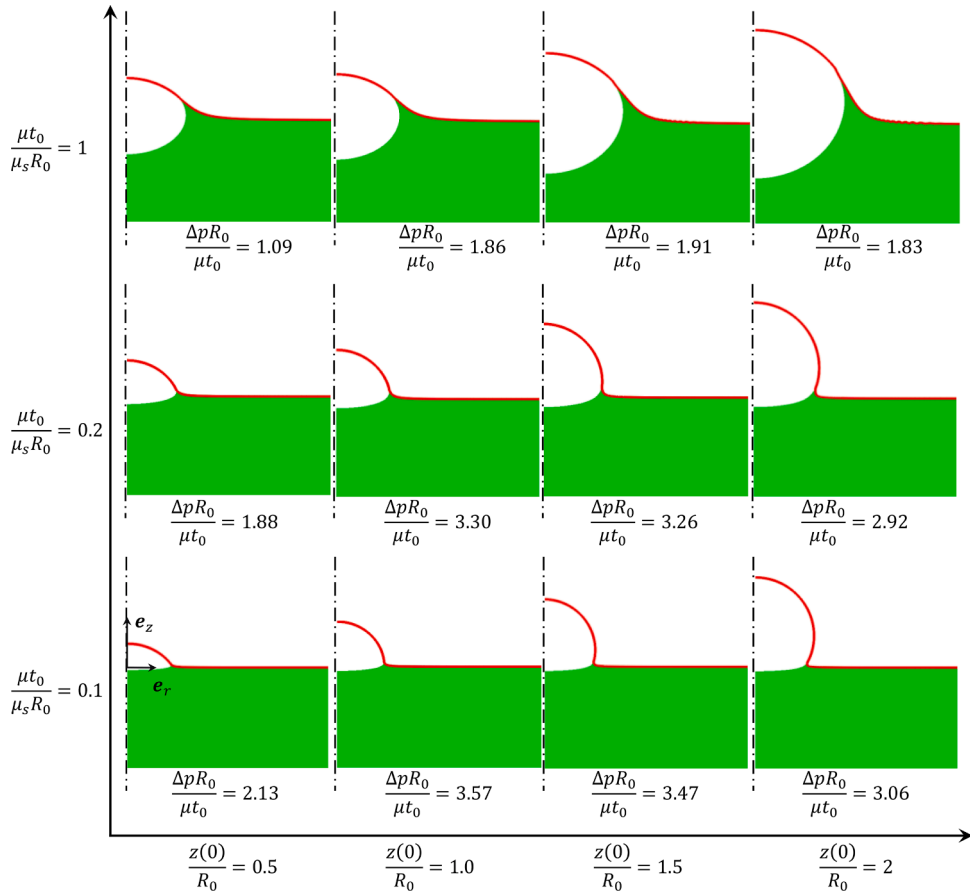


Fig. 12. FEM solutions of elastic wetting on soft substrates with various $\mu t_0/(\mu_s R_0) = 0.1, 0.2$, and 1 along the vertical axis and various aspect ratios $\frac{z(0)}{R_0} = 0.5, 1.0, 1.5$, and 2.0 along the horizontal axis.

were assumed. If the rigid substrate criterion was verified under such parameters, the criterion would be applicable for more general cases with $\gamma_{ls}, \gamma_{ms} > 0$ and $\gamma_{lm}/\mu t_0 < 1$.

Fig. 11 plots the FEM results of the normalized pressure ($\Delta p R_0/\mu t_0$) against the normalized central displacement of the membrane on a soft substrate. These results were produced by varying $\mu t_0/(\mu_s R_0)$ from 0 to 1. The black curve in Fig. 11 corresponds to $\mu t_0/(\mu_s R_0) = 0$, which represents elastic wetting on a rigid substrate. Clearly, the substrate effect on the pressure-deformation relation weakens as $\mu t_0/(\mu_s R_0)$ decreases. Particularly, when $\mu t_0/(\mu_s R_0) < 0.1$, the deviation in pressure between the soft and the rigid substrate analysis is within 6.5%. This agrees with the scaling prediction of $\mu t_0/(\mu_s R_0) \ll 1$. Fig. 12 displays the configurations of elastic wetting with $\mu t_0/(\mu_s R_0) = 0.1, 0.2$, and 1 under various aspect ratios, further indicating that the substrate deflection becomes negligible compared with the membrane deflection when $\mu t_0/(\mu_s R_0) < \sim 0.1$.

5.2. Signatures of nonlinear elastic wetting

In this section, we discuss the conditions under which the elastic wetting phenomena presented in this work are too significant to neglect.

- **Interface energy.** In Section 5.1, we have derived that the blister pressure scales as $\Delta p \sim \mu t_0 h^3/R_0^4 + \gamma h/R_0^2$. Therefore, the effect of interfacial tension would be nontrivial when $\frac{\gamma}{\mu t_0} > \sim \left(\frac{h}{R_0}\right)^2$, suggesting that systems with ultrathin and ultrasoft membranes are more likely to fall in the elastic wetting category. Such effect is especially significant in several small-scale blisters trapped by biological and soft polymer membranes (see the 8th row of Table 1).
- **Substrate stiffness.** In Section 5.1, we have derived a scaling law and verified numerically that the rigid substrate assumption could provide a good approximation when $\frac{\mu t_0}{\mu_s R_0} < \sim 0.1$. This condition is not that limited as most blisters have $t_0 \ll R_0$. Moreover, most small-scale elastic wetting systems observed in experiments satisfy this criterion (see the 10th row of Table 1).
- **Nonlinear elasticity.** Our analysis is based on both nonlinear elastic materials and nonlinear geometry, which we claimed to be significant when the aspect ratio of the blister is greater than 0.2. To justify, we compare our results with the following two typical membrane theories: the nonlinear membrane theory (without surface tension) and the Föppl-Hencky membrane theory (Hencky, 1915).

The conventional nonlinear membrane theory without surface tension is simply obtained by neglecting the interface energy term in Eq. (11) (i.e., setting $\gamma_{lm} = 0$ in Eq. (11)). The Föppl-Hencky membrane theory considers a small in-plane deformation but a relatively large deflection for the bulged membrane (also without surface tension), as well as a linear constitutive law. Therefore, the radial and hoop membrane tensions are expressed as

$$N_r = \frac{E t_0}{1 - \nu^2} (\epsilon_r + \nu \epsilon_\theta) = \frac{E t_0}{1 - \nu^2} \left[\frac{du_r}{dr} + \frac{1}{2} \left(\frac{dz}{dr} \right)^2 + \nu \frac{u_r}{r} \right], \tag{39}$$

and

$$N_\theta = \frac{E t_0}{1 - \nu^2} (\epsilon_\theta + \nu \epsilon_r) = \frac{E t_0}{1 - \nu^2} \left[\frac{u_r}{r} + \nu \frac{du_r}{dr} + \frac{\nu}{2} \left(\frac{dz}{dr} \right)^2 \right], \tag{40}$$

respectively. Here E is the Young’s modulus, ν is the Poisson’s ratio, $\epsilon_r = \frac{du_r}{dr} + \frac{1}{2} \left(\frac{dz}{dr} \right)^2$ and $\epsilon_\theta = \frac{u_r}{r}$ are the two principle in-plane strain components, u_r and z are displacements in the e_r and e_z direction, respectively. Notably, the shear modulus of the membrane is defined as $\mu = \frac{E}{2(1+\nu)}$ where $\nu = 0.5$ for the incompressible membrane.

The out-of-plane and in-plane force equilibriums based on the Föppl-Hencky membrane theory are derived as (Wang et al., 2013)

$$\begin{cases} N_r \frac{d^2 z}{dr^2} + N_\theta \frac{1}{r} \frac{dz}{dr} + \Delta p = 0, \\ \frac{dN_r}{dr} + \frac{N_r - N_\theta}{r} = 0, \end{cases} \tag{41}$$

which can also be obtained through linearizing the constitutive law and the curvature in the nonlinear membrane theory, i.e. Eq. (11).

For simplification, we adopt a clamped boundary condition in calculations. Such a boundary condition for the nonlinear membrane theory is shown in Section 2.4.2. For the Föppl-Hencky membrane theory, we consider

$$u_r(0) = \frac{dz(0)}{dr} = u_r(R_0) = z(R_0) = 0. \tag{42}$$

Eqs. (39)-(42) can be solved numerically by applying the shooting method as well. For comparison, we adopt the incompressible Gent model with $J_m = 100, 200$, and ∞ , where $J_m \rightarrow \infty$ denotes the incompressible neo-Hookean material in the nonlinear membrane theory.

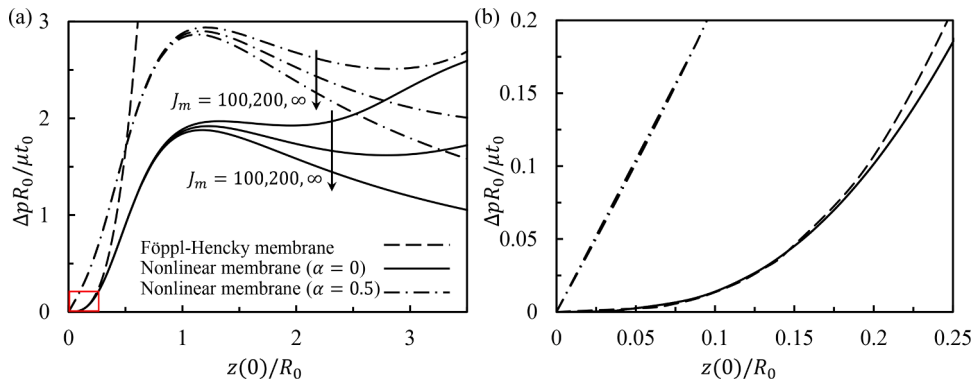


Fig. 13. (a) Normalized pressure-aspect ratio curves obtained based on our elastic wetting theory (dash-dot curves) and two conventional membrane theories without considering surface tension: the nonlinear membrane theory (solid curves) and the Föppl-Hencky membrane theory (dashed curves). (b) Zoomed-in view of the red-boxed region in (a).

Fig. 13a plots the normalized pressure-aspect ratio relations comparing the three theories and Fig. 13b offers the blown-up view of the red boxed region in Fig. 13a. We can see that the Föppl-Hencky membrane theory starts to deviate from the nonlinear membrane theory without surface tension (i.e., $\alpha = 0$) at the aspect ratio around 0.2. We, therefore, recommend that nonlinear elasticity and geometric nonlinearity should be considered when the aspect ratio of the blister is greater than 0.2. Moreover, as shown in Fig. 13, once surface tension is considered, the pressure-deformation relation is markedly affected, leading to a much higher pressure firstly, and then a more rapid pressure drop, as deformation increases. Besides, for elastic wetting with Gent membranes (i.e., $J_m = 100, 200$) and clamped boundaries, the N-shaped pressure-deformation relation is more visible in Fig. 13a than in Fig. 6a when the aspect ratio instead of the volume is adopted by the former to quantify the deformation.

Conclusions

In this paper, we model and solve the elastic wetting problems in which a droplet is confined between a soft elastic membrane and a rigid substrate at small scales such that the interplay between the interface energy and the elastic energy enriches the problem. We find that the pressure acting on the membrane-confined droplet comes from a superposition of interfacial tension (described by Young-Laplace equation) and membrane tension (controlled by nonlinear membrane theory). Though the pressure remains uniform, the membrane tension varies spatially, modifying the droplet from being in a perfectly spherical cap shape. The membrane-substrate interaction, together with the elastic and surface tensions, leads to a variety of scenarios at the contact line or the blister boundary.

This work tackles four typical boundary conditions – sliding, clamped, adhesive, and slippery boundaries. Our derivation yields two dimensionless controlling parameters in this system: the elasto-capillary number that compares the membrane-liquid surface tension with the membrane stiffness, and the effective contact angle that decays to Young's contact angle when the membrane elasticity is negligible. The essence of these complex behaviors at the contact line is explained by how the membrane tension and the elasto-capillary number modify the effective contact angle to the elastic wetting contact angle. In the adhesive case (more likely to occur in experiments), we discover that the elastic wetting contact angle is a stretch-independent constant. We therefore provide contour plots for its dependency on the two controlling parameters, which further leads to a means to experimentally measure the interface energies. We suggest that elastic wetting problems may follow the theoretical framework presented here when the elasto-capillary number is comparable with the square of the aspect ratio of the blister. We discover that the rigid substrate assumption could be satisfied when the membrane deflection is much larger than the substrate deflection, which is equivalent to $\mu t_0 / (\mu_s R_0) < \sim 0.1$. We advocate that nonlinear elasticity and geometric nonlinearity should be considered, especially when the aspect ratio is greater than 0.2. Table 1 exhibits experimentally practical parameters for the elastic wetting problems associated with biological materials, soft polymers and 2D materials, where our theory is very relevant. Our theoretical framework for elastic wetting not only enables the prediction of the blister profile and the $\Delta p - V$ relation but also provides means to experimentally extract the inner pressure as well as the interface and adhesion energies.

Declaration of Competing Interest

The authors declare that they have no known competing financial interests or personal relationships that could have appeared to influence the work reported in this paper.

The authors acknowledge the support from the US National Science Foundation (NSF), Division of Civil, Mechanical and Manufacturing Innovation (CMMI) Grant No. 1663551. We thank Professor Anand Jagota for sharing his UEL code. Y. Rao is partially supported by the China Scholarship Council (CSC). Z. Dai acknowledges the Graduate Continuing Fellowship at the University of Texas at Austin.

Supplementary materials

Supplementary material associated with this article can be found, in the online version, at [doi:10.1016/j.jmps.2021.104399](https://doi.org/10.1016/j.jmps.2021.104399).

Appendix A. Derivation of equilibrium equations and boundary conditions through energy minimization

In this section, we illustrate the derivation of the energy minimization procedure based on the calculus of variations. Firstly, substituting Eqs. (4)-(7) and (9) into Eq. (8), one obtains

$$\Pi = \int_0^{R_0} 2\pi t_0 RW(r, r', z') dR + \int_{R_0}^{\infty} 2\pi t_0 RW(r, r') dR - \Delta p \int_0^{R_0} 2\pi r r' z dR + \gamma_{lm} \int_0^{R_0} 2\pi r \sqrt{r'^2 + z'^2} dR + \gamma_{ls} \int_0^{R_0} 2\pi r r' dR + \gamma_{ms} \int_{R_0}^{\infty} 2\pi r r' dR, \tag{A.1}$$

which is rearranged as

$$\Pi = 2\pi \int_0^{R_0} F_1 dR + 2\pi \int_{R_0}^{\infty} F_2 dR, \tag{A.2}$$

where

$$F_1 = t_0 RW(r, r', z') - \Delta p r r' z + \gamma_{lm} r \sqrt{r'^2 + z'^2} + \gamma_{ls} r r',$$

$$F_2 = t_0 RW(r, r') + \gamma_{ms} r r'. \tag{A.3}$$

If we use r, z, r', z' as the variation terms, based on Eq. (10), there is

$$\delta \Pi = 2\pi \delta \int_0^{R_0^-} F_1 dR + 2\pi \delta \int_{R_0^+}^{\infty} F_2 dR = 0, \tag{A.4}$$

where R_0^- and R_0^+ represent the left (inner) and right (outer) sides of the contact line $R = R_0$, respectively.

Furthermore, based on the principle of variation, there is

$$\delta \int_0^{R_0^-} F_1 dR = \int_0^{R_0^-} \left(\frac{\partial F_1}{\partial r} \delta r + \frac{\partial F_1}{\partial r'} \delta r' + \frac{\partial F_1}{\partial z} \delta z + \frac{\partial F_1}{\partial z'} \delta z' \right) dR + F_1|_{R_0^-} \delta R_0^-, \tag{A.5}$$

where

$$\int_0^{R_0^-} \frac{\partial F_1}{\partial r'} \delta r' dR = \frac{\partial F_1}{\partial r'}|_{R_0^-} (\delta r)(R_0^-) - \frac{\partial F_1}{\partial r'}|_0 (\delta r)(0) - \int_0^{R_0^-} \frac{d}{dR} \frac{\partial F_1}{\partial r'} \delta r dR,$$

$$\int_0^{R_0^-} \frac{\partial F_1}{\partial z'} \delta z' dR = \frac{\partial F_1}{\partial z'}|_{R_0^-} (\delta z)(R_0^-) - \frac{\partial F_1}{\partial z'}|_0 (\delta z)(0) - \int_0^{R_0^-} \frac{d}{dR} \frac{\partial F_1}{\partial z'} \delta z dR. \tag{A.6}$$

Similarly, there is

$$\delta \int_{R_0^+}^{\infty} F_2 dR = \int_{R_0^+}^{\infty} \left(\frac{\partial F_2}{\partial r} \delta r + \frac{\partial F_2}{\partial r'} \delta r' \right) dR - F_2|_{R_0^+} \delta R_0^+, \tag{A.7}$$

where

$$\int_{R_0^+}^{\infty} \frac{\partial F_2}{\partial r'} \delta r' dR = \frac{\partial F_2}{\partial r'}|_{\infty} (\delta r)(\infty) - \frac{\partial F_2}{\partial r'}|_{R_0^+} (\delta r)(R_0^+) - \int_{R_0^+}^{\infty} \frac{d}{dR} \frac{\partial F_2}{\partial r'} \delta r dR. \tag{A.8}$$

Based on the above, we plug Eqs. (A.5)–(A.8) into Eq. (A.4), yielding

$$\begin{aligned}
 & \int_0^{R_0^-} \left(\left(\frac{\partial F_1}{\partial r} - \frac{d}{dR} \frac{\partial F_1}{\partial r'} \right) \delta r + \left(\frac{\partial F_1}{\partial z} - \frac{d}{dR} \frac{\partial F_1}{\partial z'} \right) \delta z \right) dR \\
 & + F_1|_{R_0^-} \delta R_0^- + \frac{\partial F_1}{\partial r'}|_{R_0^-} (\delta r)(R_0^-) + \frac{\partial F_1}{\partial z'}|_{R_0^-} (\delta z)(R_0^-) - \frac{\partial F_1}{\partial r'}|_0 (\delta r)(0) \\
 & - \frac{\partial F_1}{\partial z'}|_0 (\delta z)(0) + \int_{R_0^+}^{\infty} \left(\left(\frac{\partial F_2}{\partial r} - \frac{d}{dR} \frac{\partial F_2}{\partial r'} \right) \delta r \right) dR \\
 & - F_2|_{R_0^+} \delta R_0^+ + \frac{\partial F_2}{\partial r'}|_{\infty} (\delta r)(\infty) - \frac{\partial F_2}{\partial r'}|_{R_0^+} (\delta r)(R_0^+) = 0.
 \end{aligned} \tag{A.9}$$

To satisfy Eq. (A.9), one obtains

$$\begin{cases} \frac{\partial F_1}{\partial r} - \frac{d}{dR} \frac{\partial F_1}{\partial r'} = 0 \\ \frac{\partial F_1}{\partial z} - \frac{d}{dR} \frac{\partial F_1}{\partial z'} = 0 \end{cases} \quad \forall 0 \leq R \leq R_0^-, \tag{A.10}$$

and

$$\frac{\partial F_2}{\partial r} - \frac{d}{dR} \frac{\partial F_2}{\partial r'} = 0 \quad \forall R \geq R_0^+. \tag{A.11}$$

In addition, plugging Eq. (A.3) into Eq. (A.10), one obtains

$$\begin{cases} t_0 \left[R \frac{\partial W}{\partial r} - \left(R \frac{\partial W}{\partial r'} \right)' \right] - \Delta p [r'z - (rz)'] + \gamma_{lm} \left[\sqrt{r'^2 + z'^2} - \left(\frac{rr'}{\sqrt{r'^2 + z'^2}} \right)' \right] = 0 \\ t_0 \left[R \frac{\partial W}{\partial z} - \left(R \frac{\partial W}{\partial z'} \right)' \right] - \Delta p r r' - \gamma_{lm} \left(\frac{r z'}{\sqrt{r'^2 + z'^2}} \right)' = 0 \end{cases} \quad \forall 0 \leq R \leq R_0^-. \tag{A.12}$$

Similarly, plugging Eq. (A.3) into (A.11), one obtains

$$t_0 \left[R \frac{\partial W}{\partial r} - \left(R \frac{\partial W}{\partial r'} \right)' \right] = 0 \quad \forall R \geq R_0^+. \tag{A.13}$$

Besides, based on Eq. (1), there is

$$\frac{\partial W}{\partial r} = \frac{1}{R} \frac{\partial W}{\partial \lambda_\theta}, \frac{\partial W}{\partial r'} = \frac{r'}{\lambda_r} \frac{\partial W}{\partial \lambda_r}, \frac{\partial W}{\partial z} = 0, \frac{\partial W}{\partial z'} = \frac{z'}{\lambda_r} \frac{\partial W}{\partial \lambda_r}. \tag{A.14}$$

Now, combining with Eqs. (13) and (A.14), Eq. (A.12) can be rewritten as

$$\begin{cases} \Delta p = -\frac{t_0}{r z'} \left[\frac{\partial W}{\partial \lambda_\theta} - \frac{r'}{\lambda_r} \frac{\partial W}{\partial \lambda_r} - R \left(\frac{r'}{\lambda_r} \right)' \frac{\partial W}{\partial \lambda_r} - R \frac{r'}{\lambda_r} \left(\frac{\partial W}{\partial \lambda_r} \right)' \right] - \gamma_{lm} (\kappa_r + \kappa_\theta) \\ \Delta p = \frac{t_0}{r r'} \left[-\frac{\partial W}{\partial \lambda_r} \left(R \frac{z'}{\lambda_r} \right)' - R \frac{z'}{\lambda_r} \left(\frac{\partial W}{\partial \lambda_r} \right)' \right] - \gamma_{lm} (\kappa_r + \kappa_\theta) \end{cases} \quad \forall 0 \leq R \leq R_0^-. \tag{A.15}$$

Similarly, Eq. (A.13) can be rewritten as

$$\frac{\partial W}{\partial \lambda_\theta} - \frac{r'}{\lambda_r} \frac{\partial W}{\partial \lambda_r} - R \left(\frac{r'}{\lambda_r} \right)' \frac{\partial W}{\partial \lambda_r} - R \frac{r'}{\lambda_r} \left(\frac{\partial W}{\partial \lambda_r} \right)' = 0 \quad \forall R \geq R_0^+. \tag{A.16}$$

By computing the difference between the two equations in Eq. (A.15) and then combining with Eq. (14), one obtains

$$\frac{dN_r}{dR} + \frac{r'(N_r - N_\theta)}{r} = 0 \quad \forall 0 \leq R \leq R_0^-. \tag{A.17}$$

Meanwhile, by computing the average between two equations in Eq. (A.15) and then combining with Eq. (14), one obtains

$$\kappa_r N_r + \kappa_\theta N_\theta + \gamma_{lm} (\kappa_r + \kappa_\theta) + \Delta p = 0 \quad \forall 0 \leq R \leq R_0^-. \tag{A.18}$$

As we can see, Eqs. (A.17)-(A.18) are the equilibrium equations at the inner side of the membrane-confined droplet, shown as Eq. (11).

Combining with Eq. (14), Eq. (A.16) is expressed as

$$\frac{dN_r}{dR} + \frac{r'(N_r - N_\theta)}{r} = 0 \quad \forall R \geq R_0^+, \tag{A.19}$$

which is the equilibrium equation at the outside of the membrane-confined droplet, shown as Eq. (12).

Now, the residual parts in Eq. (A.9) are considered as boundary terms, which is

$$\begin{aligned} F_1|_{R_0^-} \delta R_0^- + \frac{\partial F_1}{\partial r'} \Big|_{R_0^-} (\delta r)(R_0^-) + \frac{\partial F_1}{\partial z'} \Big|_{R_0^-} (\delta z)(R_0^-) - \frac{\partial F_1}{\partial r'} \Big|_0 (\delta r)(0) - \frac{\partial F_1}{\partial z'} \Big|_0 (\delta z)(0) - F_2|_{R_0^+} \delta R_0^+ + \\ \frac{\partial F_2}{\partial r'} \Big|_\infty (\delta r)(\infty) - \frac{\partial F_2}{\partial r'} \Big|_{R_0^+} (\delta r)(R_0^+) = 0. \end{aligned} \tag{A.20}$$

We know that

$$\begin{aligned} \delta R_0^- = \delta R_0^+ = \delta R_0, \delta r(R_0^-) = \delta r(R_0^+) = \delta r_0, \delta z(R_0^-) = \delta z(R_0^+) = \delta z_0, \\ (\delta r)(R_0^\pm) = \delta r(R_0^\pm) - (r')|_{R_0^\pm} \delta R_0^\pm = \delta r_0 - (r')|_{R_0^\pm} \delta R_0, \\ (\delta z)(R_0^\pm) = \delta z(R_0^\pm) - (z')|_{R_0^\pm} \delta R_0^\pm = \delta z_0 - (z')|_{R_0^\pm} \delta R_0, \\ (\delta r)(0) = \delta r(0) - r'(0)\delta 0 = 0, (\delta z)(0) = \delta z(0) - z'(0)\delta 0 = \delta z(0), \\ (\delta r)(\infty) = \delta r(\infty) - r'(\infty)\delta(\infty) = \delta r(\infty). \end{aligned} \tag{A.21}$$

Therefore, by plugging Eqs. (A.3) and (A.21) into Eq. (A.20), one obtains

$$\begin{aligned} \left[t_0 R W - \Delta p r r' z + \gamma_{lm} r \sqrt{r'^2 + z'^2} + \gamma_{ls} r r' \right] \Big|_{R_0^-} \delta R_0 + \left[t_0 R \frac{\partial W}{\partial r'} - \Delta p r z + \gamma_{lm} \frac{r r'}{\sqrt{r'^2 + z'^2}} + \gamma_{ls} r \right] \Big|_{R_0^-} (\delta r_0 - (r')|_{R_0^-} \delta R_0) \\ + \left[t_0 R \frac{\partial W}{\partial z'} + \gamma_{lm} \frac{r z'}{\sqrt{r'^2 + z'^2}} \right] \Big|_{R_0^-} (\delta z_0 - (z')|_{R_0^-} \delta R_0) - \left[t_0 R \frac{\partial W}{\partial z'} + \gamma_{lm} \frac{r z'}{\sqrt{r'^2 + z'^2}} \right] \Big|_0 \delta z(0) - \\ \left[t_0 R W + \gamma_{ms} r r' \right] \Big|_{R_0^+} \delta R_0 - \left[t_0 R \frac{\partial W}{\partial r'} + \gamma_{ms} r \right] \Big|_{R_0^+} (\delta r_0 - (r')|_{R_0^+} \delta R_0) + \left[t_0 R \frac{\partial W}{\partial r'} + \gamma_{ms} r \right] \Big|_\infty \delta r(\infty) = 0. \end{aligned} \tag{A.22}$$

Based on Eqs. (1), (2), (14), (19), and (A.14), we simplify it as Eq. (17). By now, all the equilibrium equations and boundary conditions are derived for elastic wetting.

Appendix B. Shooting method

We adopted shooting method to numerically solve the ODE system consisting of the equilibrium Eq. (11) and various boundary conditions given in Section 2.4. Instead of solving 2nd order ODEs for z and r , we solve 1st order ODEs for $\lambda_\theta, \lambda_r, z, \phi$. To do so, We plug Eq. (2) into Eq. (13), yielding

$$\kappa_r = -\frac{\phi'}{\lambda_r}, \quad \kappa_\theta = -\frac{\sin \phi}{r}. \tag{B.1}$$

Combining with Eq. (B.1), Eq. (11) can be then rewritten as

$$\begin{cases} \phi' = \frac{-(N_\theta + \gamma_{lm}) \frac{\lambda_r}{\lambda_\theta} \frac{\sin \phi}{R} + \Delta p \lambda_r}{N_r + \gamma_{lm}} \\ \lambda_r' = \frac{-\cos \phi \lambda_r \left(\frac{\partial N_r}{\partial \lambda_\theta} + \frac{N_r - N_\theta}{\lambda_\theta} \right) + \frac{\partial N_r}{\partial \lambda_\theta} \frac{\lambda_\theta}{R}}{\frac{\partial N_r}{\partial \lambda_r}} \end{cases} \tag{B.2}$$

Next, plugging Eq. (15) into Eq. (14), we express the in-plane membrane tractions for neoHookean materials in terms of principal stretches as

$$\begin{cases} N_r = \frac{\mu t_0 (\lambda_r^4 \lambda_\theta^2 - 1)}{\lambda_r^3 \lambda_\theta^3} \\ N_\theta = \frac{\mu t_0 (\lambda_r^2 \lambda_\theta^4 - 1)}{\lambda_r^3 \lambda_\theta^3} \end{cases} \tag{B.3}$$

Similarly, for Gent materials, plugging Eq. (16) in Eq. (14), one obtains

$$\begin{cases} N_r = \frac{-\mu t_0 J_m (\lambda_r^4 \lambda_\theta^2 - 1)}{\lambda_r \lambda_\theta + \lambda_r^3 \lambda_\theta^3 (\lambda_r^2 + \lambda_\theta^2 - 3 - J_m)} \\ N_\theta = \frac{-\mu t_0 J_m (\lambda_r^2 \lambda_\theta^4 - 1)}{\lambda_r \lambda_\theta + \lambda_r^3 \lambda_\theta^3 (\lambda_r^2 + \lambda_\theta^2 - 3 - J_m)} \end{cases} \tag{B.4}$$

A shooting method can be constructed using the terms $\{y_1, y_2, y_3, y_4\} = \{\lambda_\theta, z/R_0, \phi, \lambda_r\}$ as variables for the corresponding boundary value problem. Based on Eqs. (2) and (B.3), we have the computational equations based on the incompressible neo-Hookean material model as

$$\begin{cases} \frac{d}{d\widehat{R}} y_1 = \frac{y_4 \cos y_3 - y_1}{\widehat{R}} \\ \frac{d}{d\widehat{R}} y_2 = -y_4 \sin y_3 \\ \frac{d}{d\widehat{R}} y_3 = -\frac{y_4 [y_4^2 y_1^4 - 1 + \alpha y_4^3 y_1^3] \frac{\sin y_3}{\widehat{R}} - \frac{\Delta p R_0}{\mu t_0} y_4^4 y_1^4}{y_1 (y_4^2 y_1^2 - 1 + \alpha y_4^3 y_1^3)}, \\ \frac{d}{d\widehat{R}} y_4 = \frac{y_4^2 (y_4^2 y_1^4 - 3) \cos y_3 - y_4 y_1 (y_4^2 y_1^2 - 3)}{\widehat{R} y_1 (y_4^2 y_1^2 + 3)} \end{cases} \tag{B.5}$$

where $\widehat{R} = R/R_0$ and $\alpha = \gamma_{lm}/\mu t_0$. Similarly, based on Eqs. (2) and (B.4), the computational equations based on the incompressible Gent material model are expressed as

$$\begin{cases} \frac{d}{d\widehat{R}} y_1 = \frac{y_4 \cos y_3 - y_1}{\widehat{R}} \\ \frac{d}{d\widehat{R}} y_2 = -y_4 \sin y_3 \\ \frac{d}{d\widehat{R}} y_3 = -\frac{y_4 [y_4^2 y_1^4 - 1 + \alpha y_4^3 y_1^3 \delta] \frac{\sin y_3}{\widehat{R}} - \frac{\Delta p R_0}{\mu t_0} y_4^4 y_1^4 \delta}{y_1 (y_4^2 y_1^2 - 1 + \alpha y_4^3 y_1^3 \delta)}, \\ \frac{d}{d\widehat{R}} y_4 = \delta \frac{y_4^2 (y_4^2 y_1^4 - 3) \cos y_3 - y_4 y_1 (y_4^2 y_1^2 - 3)}{\widehat{R} y_1 \left[(y_4^2 y_1^2 + 3) \delta + \frac{2(y_4^2 y_1^2 - 1)^2}{J_m \lambda_{41}^2} \right]} + \frac{2y_4 (y_4^6 y_1^6 - y_4^2 y_1^2 I_1 + 2) (-y_4 \cos y_3 + y_1)}{\widehat{R} y_1 [y_4^2 y_1^2 (y_4^2 y_1^2 + 3) J_m \delta + 2(y_4^2 y_1^2 - 1)^2]} \end{cases} \tag{B.6}$$

where $\delta = 1 - (I_1 - 3)/J_m$.

In addition, the initial conditions of Eqs. (B.5) and (B.6) at $\widehat{R} = 0$ are summarized as

$$y_1(0) = k, \quad y_2(0) = 0, \quad y_3(0) = 0 \text{ and } y_4(0) = k, \tag{B.7}$$

where k is varied until boundary conditions at $\widehat{R} = 1$ are satisfied. Notably, although the central height of a specific blister system (i.e., $y_2(0)$) is an unknown constant physically, assigning $y_2(0) = 0$ is reasonable in computation because the value of y_2 is independent with the computation of y_1, y_3 and y_4 . Besides, to avoid numerical singularity at $\widehat{R} = 0$, the solution procedure may start at a sufficiently small value, i.e., $\widehat{R} = \epsilon \ll 1$, so that the initial conditions are reformulated as

$$y_1(\epsilon) = k, \quad y_2(\epsilon) = 0,$$

$$y_3(\epsilon) = \frac{\frac{\Delta p R_0}{\mu_0} k^7 g(k)}{k^6 - 1 + \alpha k^6 g(k)} \epsilon, \quad y_4(\epsilon) = k, \tag{B.8}$$

where $g(k) = 1$ for neo-Hookean materials and $g(k) = 1 - (2k^6 - 3k^4 + 1)/(J_m k^4)$ for Gent materials. Combining with boundary conditions discussed in Section 2.4, the elastic wetting problem with neo-Hookean material can be resolved by computing Eq. (B.5); and the elastic wetting problem with Gent material can be resolved by computing Eq. (B.6). The numerical solver is coded in Matlab using $\epsilon = 10^{-5}$, which is based on a basic convergence study.

Appendix C. Numerical results for elastic wetting with Gent membranes

Figs. C1–C7.

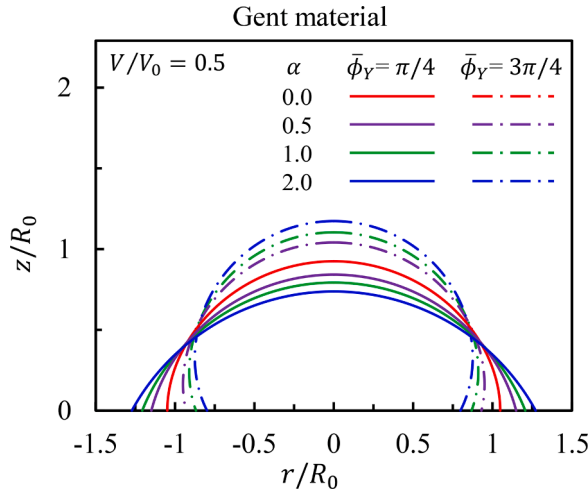


Fig. C1. Profiles of droplets confined by Gent membranes subjected to sliding boundary conditions. $V/V_0 = 0.5$ is prescribed while the elastocapillary numbers α is varying. Solid curves correspond to $\bar{\phi}_Y = \pi/4$ and dash-dot curves for $\bar{\phi}_Y = 3\pi/4$. The two red curves overlay.

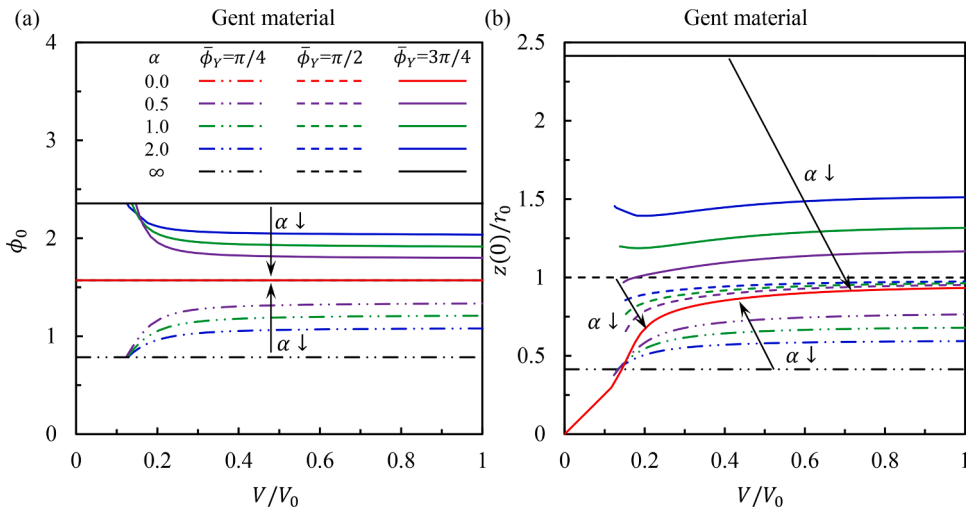


Fig. C2. The evolution of (a) the elastic wetting contact angle and (b) the aspect ratio of droplets confined by Gent membranes subjected to sliding boundary conditions for $\bar{\phi}_Y = \pi/4$ (dash-dot-dot curves), $\pi/2$ (dashed curves) and $3\pi/4$ (solid curves) with various α . The arrows indicate α decreases from ∞ to 0 . In (a), all the dashed curves and red curves (i.e., when $\bar{\phi}_Y = \pi/2$ or $\alpha = 0$) collapse to the red solid line. In (b), all the red curves (i.e., when $\alpha = 0$) collapse to the red solid curve.

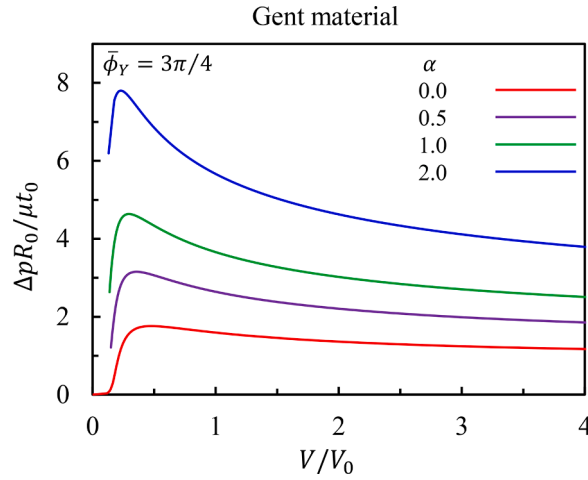


Fig. C3. Normalized pressure-deformation relations for elastic wetting with Gent membranes and sliding boundaries under various elasto-capillary numbers α .

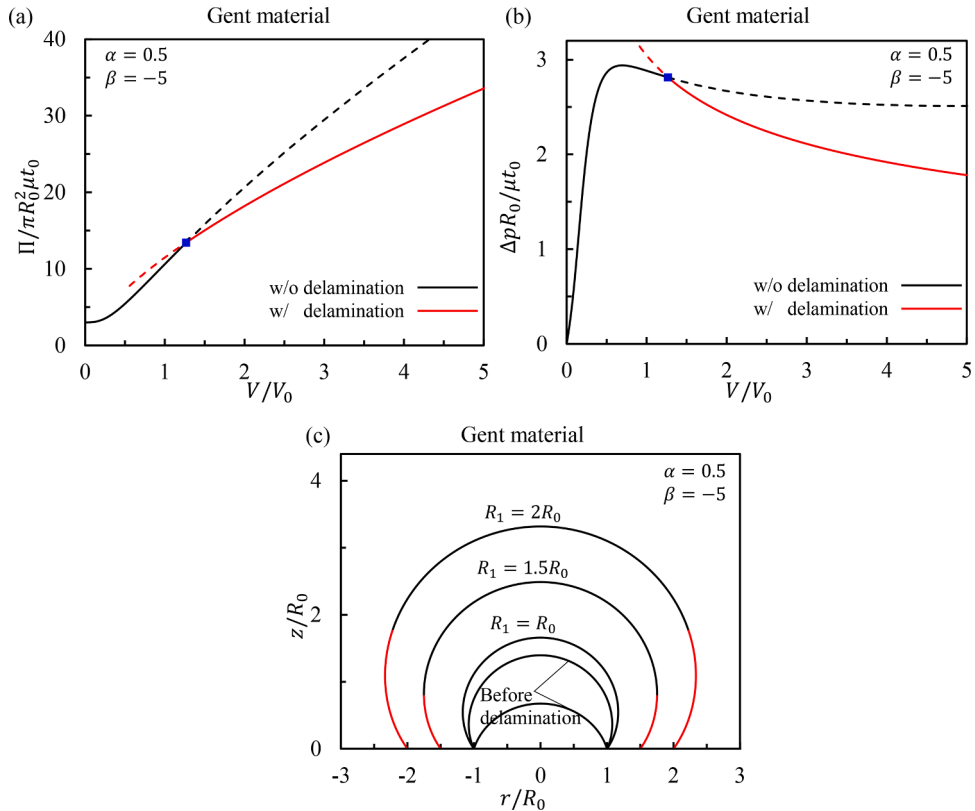


Fig. C4. Normalized (a) free energy-deformation and (b) pressure-deformation relations for elastic wetting with a Gent membrane and an adhesive boundary when $\alpha = 0.5$ and $\beta = -5$ are given. The black and red curves represent configurations without and with edge delamination, respectively. The solid curves represent the actual evolution pathways of free energy/pressure. The blue marker at the intersection of the black and red curves highlights the critical volume-to-delaminate. (c) The growth of the blister profile under the adhesive boundary. The black and red parts represent the sections of the membrane that are initially detached from or attached to the substrate before any liquid injection. In other words, the red parts are delaminated membrane due to the increased liquid volume. For the two blister profiles labeled with “before delamination”, their prescribed volumes are $V/V_0 = 0.3$ and 0.9 .

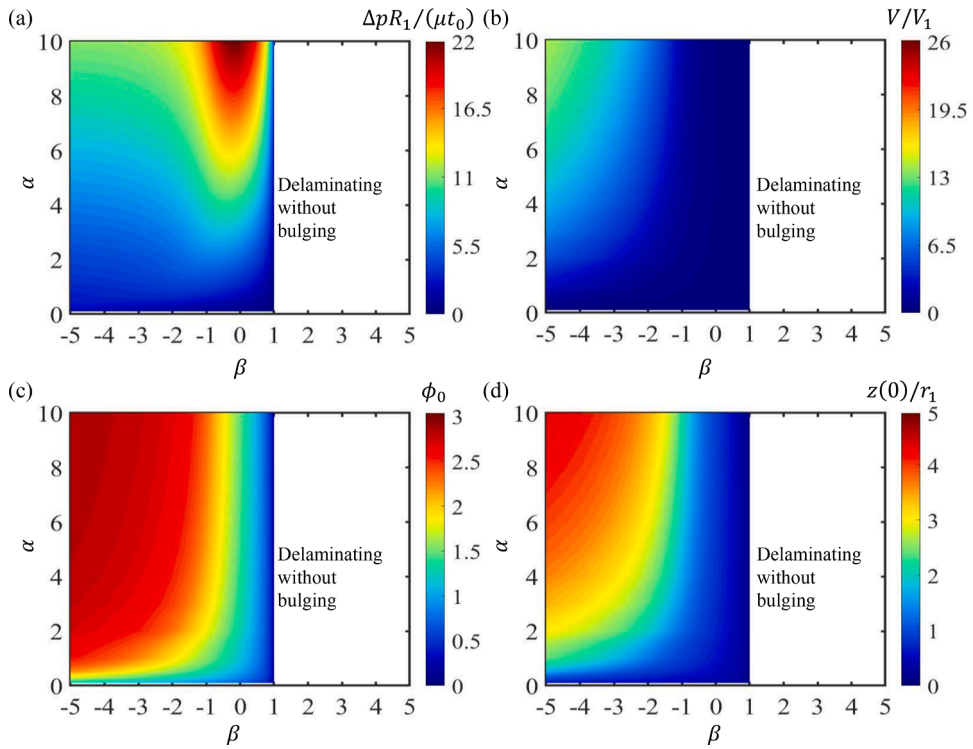


Fig. C5. Contour plots of (a) the normalized pressure, (b) the normalized volume, (c) the elastic wetting contact angle, and (d) the aspect ratio in $\alpha \sim \beta$ parametric space for elastic wetting with Gent membranes and adhesive boundaries.

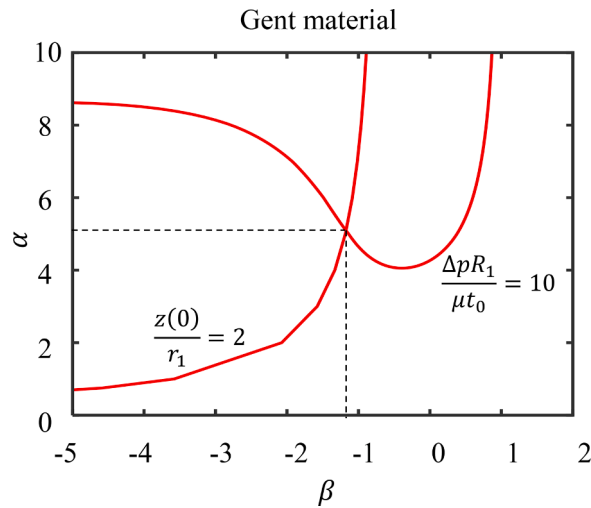


Fig. C6. Contour curves for $z(0)/r_1 = 2$ and $\Delta pR_1/\mu t_0 = 10$ in $\alpha \sim \beta$ parametric space for elastic wetting with a Gent membrane and an adhesive boundary.

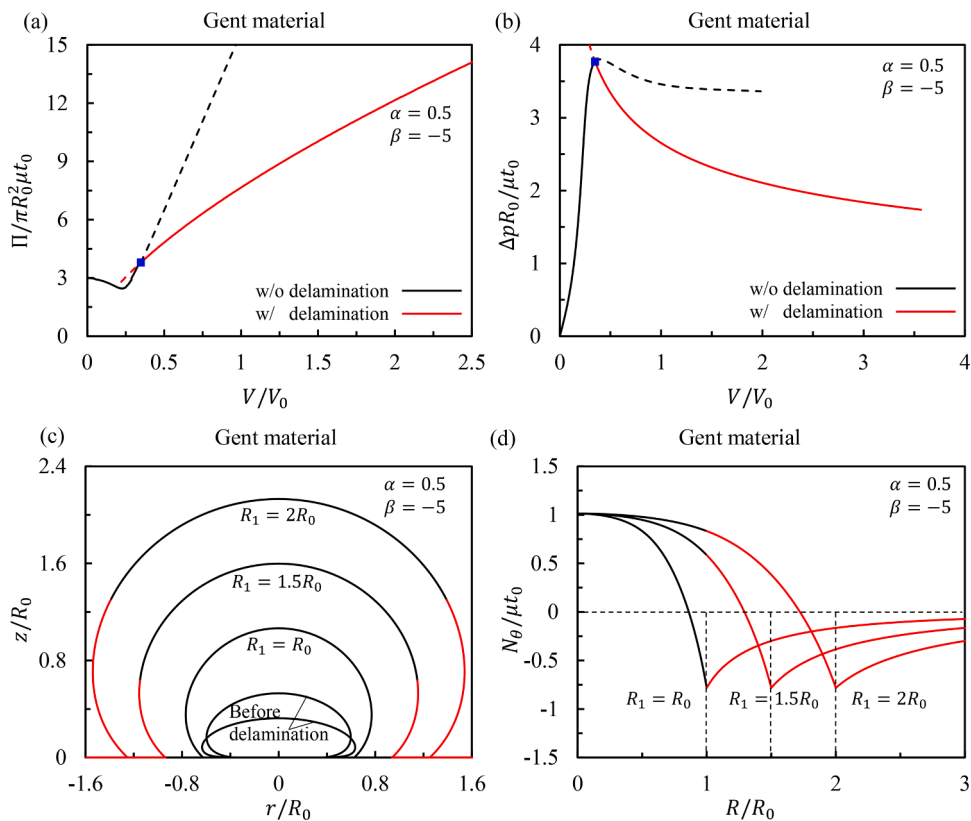


Fig. C7. Normalized (a) free energy-deformation and (b) pressure-deformation relations for elastic wetting with a Gent membrane and a slippery boundary when $\alpha = 0.5$ and $\beta = -5$ are given. The black and red curves represent configurations without and with edge delamination, respectively. (c) The growth of the blister profile under the slippery boundary. The black and red parts represent the sections of the membrane that are initially detached from or attached to the substrate before any liquid injection. For the two blister profiles before delamination, their prescribed volumes are $V/V_0 = 0.1$ and 0.2 . (d) Normalized hoop tension in the membrane with edge delamination of $R_1 = R_0$, $1.5R_0$, and $2R_0$.

References

- Antkowiak, A., Audoly, B., Jossierand, C., Neukirch, S., Rivetti, M., 2011. Instant fabrication and selection of folded structures using drop impact. *Proc. Natl. Acad. Sci.* 108, 10400.
- Benet, E., Vernerey, F.J., 2019. Dynamic competition of inflation and delamination in the finite deformation of thin membranes. *Soft Matter* 15, 6630–6641.
- Bico, J., Reyssat, É., Roman, B., 2018. Elastocapillarity: when surface tension deforms elastic solids. *Annu. Rev. Fluid Mech.* 50, 629–659.
- Blossey, R., 2003. Self-cleaning surfaces — virtual realities. *Nat. Mater.* 2, 301–306.
- Calvimontes, A., 2017. The measurement of the surface energy of solids using a laboratory drop tower. *npj Microgravity* 3, 25.
- Cao, Z., Tao, L., Akinwande, D., Huang, R., Liechti, K.M., 2015. Mixed-mode interactions between graphene and substrates by blister tests. *J. Appl. Mech.* 82.
- Cao, Z., Wang, P., Gao, W., Tao, L., Suk, J.W., Ruoff, R.S., Akinwande, D., Huang, R., Liechti, K.M., 2014. A blister test for interfacial adhesion of large-scale transferred graphene. *Carbon* 69, 390–400.
- Charras, G.T., 2008. A short history of blebbing. *J. Microsc.* 231, 466–478.
- Chopin, J., Vella, D., Boudaoud, A., 2008. The liquid blister test. *Proc. R. Soc. A: Math. Phys. Eng. Sci.* 464, 2887–2906.
- Dai, Z., Hou, Y., Sanchez, D.A., Wang, G., Brennan, C.J., Zhang, Z., Liu, L., Lu, N., 2018. Interface-governed deformation of nanobubbles and nanotents formed by two-dimensional materials. *Phys. Rev. Lett.* 121, 266101.
- Dai, Z., Liu, L., Zhang, Z., 2019. Strain engineering of 2D materials: issues and opportunities at the interface. *Adv. Mater.* 31, 1805417.
- Dai, Z., Lu, N., 2021. Poking and bulging of suspended thin sheets: slippage, instabilities, and metrology. *J. Mech. Phys. Solids* 149, 104320.
- Dai, Z., Lu, N., Liechti, K.M., Huang, R., 2020a. Mechanics at the interfaces of 2D materials: challenges and opportunities. *Curr. Opin. Solid State Mater. Sci.* 24, 100837.
- Dai, Z., Sanchez, D.A., Brennan, C.J., Lu, N., 2020b. Radial buckle delamination around 2D material tents. *J. Mech. Phys. Solids* 137, 103843.
- Dannenberg, H., 1961. Measurement of adhesion by a blister method. *J. Appl. Polym. Sci.* 5, 125–134.
- Davidovitch, B., Vella, D., 2018. Partial wetting of thin solid sheets under tension. *Soft Matter* 14, 4913–4934.
- De Gennes, P.-G., Brochard-Wyart, F., Quéré, D., 2013. *Capillarity and Wetting Phenomena: Drops, Bubbles, Pearls, Waves*. Springer Science & Business Media.
- de Langre, E., Baroud, C.N., Reverdy, P., 2010. Energy criteria for elasto-capillary wrapping. *J. Fluids Struct.* 26, 205–217.
- Dimova, R., Lipowsky, R., 2012. Lipid membranes in contact with aqueous phases of polymer solutions. *Soft Matter* 8, 6409–6415.
- Fernández-Toledano, J.C., Braeckveldt, B., Marengo, M., De Coninck, J., 2020. How wettability controls nanoprinting. *Phys. Rev. Lett.* 124, 224503.
- Gent, A.N., 1996. A new constitutive relation for rubber. *Rubber Chem. Technol.* 69, 59–61.
- Gent, A.N., 2005. Elastic instabilities in rubber. *Int. J. Non Linear Mech.* 40, 165–175.
- Gent, A.N., Lewandowski, L.H., 1987. Blow-off pressures for adhering layers. *J. Appl. Polym. Sci.* 33, 1567–1577.
- Ghorbanfekr-Kalashami, H., Vasu, K.S., Nair, R.R., Peeters, F.M., Neek-Amal, M., 2017. Dependence of the shape of graphene nanobubbles on trapped substance. *Nat. Commun.* 8, 15844.

- Gilcreest, V.P., Carroll, W.M., Rochev, Y.A., Blute, I., Dawson, K.A., Gorelov, A.V., 2004. Thermoresponsive poly(*n*-isopropylacrylamide) copolymers: contact angles and surface energies of polymer films. *Langmuir* 20, 10138–10145.
- Hencky, H., 1915. On the stress state in circular plates with vanishing bending stiffness. *Zeitschr. Math. Phys.* 63, 311–317.
- Hohlfelder, R.J., Luo, H., Vlassak, J.J., Chidsey, C.D., Nix, W.D., 1996. Measuring interfacial fracture toughness with the blister test. In: *MRS Online Proceedings Library Archive*, p. 436.
- Huang, J., Juszkiewicz, M., de Jeu, W.H., Cerda, E., Emrick, T., Menon, N., Russell, T.P., 2007. Capillary wrinkling of floating thin polymer films. *Science* 317, 650.
- Jagota, A., Argento, C., Mazur, S., 1998. Growth of adhesive contacts for Maxwell viscoelastic spheres. *J. Appl. Phys.* 83, 250–259.
- Jensen, H.M., 1991. The blister test for interface toughness measurement. *Eng. Fract. Mech.* 40, 475–486.
- Khestanova, E., Guinea, F., Fumagalli, L., Geim, A.K., Grigorieva, I.V., 2016. Universal shape and pressure inside bubbles appearing in van der Waals heterostructures. *Nat. Commun.* 7, 12587.
- Knoche, S., Vella, D., Aumaitre, E., Degen, P., Rehage, H., Cicuta, P., Kierfeld, J., 2013. Elastometry of deflated capsules: elastic moduli from shape and wrinkle analysis. *Langmuir* 29, 12463–12471.
- Kwok, D.Y., Lam, C.N.C., Li, A., Zhu, K., Wu, R., Neumann, A.W., 1998. Low-rate dynamic contact angles on polystyrene and the determination of solid surface tensions. *Polym. Eng. Sci.* 38, 1675–1684.
- Latorre, E., Kale, S., Casares, L., Gómez-González, M., Uroz, M., Valon, L., Nair, R.V., Garreta, E., Montserrat, N., del Campo, A., Ladoux, B., Arroyo, M., Trepát, X., 2018. Active superelasticity in three-dimensional epithelia of controlled shape. *Nature* 563, 203–208.
- Lim, C.H.Y.X., Nesladek, M., Loh, K.P., 2014. Observing high-pressure chemistry in graphene bubbles. *Angew. Chem. Int. Ed.* 53, 215–219.
- Liu, T., Liu, Z., Jagota, A., Hui, C.-Y., 2020. Droplets on an elastic membrane: configurational energy balance and modified Young equation. *J. Mech. Phys. Solids* 138, 103902.
- Lubarda, V.A., 2013. Circular loads on the surface of a half-space: displacement and stress discontinuities under the load. *Int. J. Solids Struct.* 50, 1–14.
- Paulsen, J.D., Démyer, V., Santangelo, C.D., Russell, T.P., Davidovitch, B., Menon, N., 2015. Optimal wrapping of liquid droplets with ultrathin sheets. *Nat. Mater.* 14, 1206–1209.
- Quéré, D., di Meglio, J.-M., Brochard-Wyart, F., 1990. Spreading of liquids on highly curved surfaces. *Science* 249, 1256.
- Rivlin, R.S., Taylor, G.I., 1948. Large elastic deformations of isotropic materials. I. Fundamental concepts. *Philos. Trans. R. Soc. London. Ser. A, Math. Phys. Sci.* 240, 459–490.
- Roman, B., Bico, J., 2010. Elasto-capillarity: deforming an elastic structure with a liquid droplet. *J. Phys. Condens. Matter* 22, 493101.
- Sanchez, D.A., Dai, Z., Lu, N., 2021. 2D Material Bubbles: Fabrication, Characterization, and Applications. *Trends in Chemistry*.
- Sanchez, D.A., Dai, Z., Wang, P., Cantu-Chavez, A., Brennan, C.J., Huang, R., Lu, N., 2018. Mechanics of spontaneously formed nanoblisters trapped by transferred 2D crystals. *Proc. Natl. Acad. Sci.* 115, 7884.
- Schulman, R.D., Dalnoki-Veress, K., 2018. Droplets capped with an elastic film can be round, elliptical, or nearly square. *Phys. Rev. Lett.* 121, 248004.
- Schulman, R.D., Trejo, M., Salez, T., Raphaël, E., Dalnoki-Veress, K., 2018. Surface energy of strained amorphous solids. *Nat. Commun.* 9, 982.
- Shen, T., Kan, J., Benet, E., Vernerey, F.J., 2019. On the blistering of thermo-sensitive hydrogel: the volume phase transition and mechanical instability. *Soft Matter* 15, 5842–5853.
- Shimizu, R.N., Demarquette, N.R., 2000. Evaluation of surface energy of solid polymers using different models. *J. Appl. Polym. Sci.* 76, 1831–1845.
- Shuttleworth, R., 1950. The surface tension of solids. *Proc. Phys. Soc. London Sect. A* 63, 444–457.
- Style, R.W., Jagota, A., Hui, C.-Y., Dufresne, E.R., 2017. Elastocapillarity: surface tension and the mechanics of soft solids. *Annu. Rev. Condens. Matter Phys.* 8, 99–118.
- Temmen, M., Ochedowski, O., Schleberger, M., Reichling, M., Bollmann, T.R.J., 2014. Hydration layers trapped between graphene and a hydrophilic substrate. *N. J. Phys.* 16, 053039.
- Vlassak, J.J., Nix, W.D., 1992. A new bulge test technique for the determination of Young's modulus and Poisson's ratio of thin films. *J. Mater. Res.* 7, 3242–3249.
- Wang, F., Yuan, C., Lu, T., Wang, T.J., 2017a. Anomalous bulging behaviors of a dielectric elastomer balloon under internal pressure and electric actuation. *J. Mech. Phys. Solids* 102, 1–16.
- Wang, G., Dai, Z., Wang, Y., Tan, P., Liu, L., Xu, Z., Wei, Y., Huang, R., Zhang, Z., 2017b. Measuring interlayer shear stress in bilayer graphene. *Phys. Rev. Lett.* 119, 036101.
- Wang, P., Gao, W., Cao, Z., Liechti, K.M., Huang, R., 2013. Numerical analysis of circular graphene bubbles. *J. Appl. Mech.* 80.
- Wang, S., Zhang, Y., Abidi, N., Cabrales, L., 2009. Wettability and surface free energy of graphene films. *Langmuir* 25, 11078–11081.
- Wu, S., 1971. Calculation of interfacial tension in polymer systems. *J. Polym. Sci. Part C* 34, 19–30.
- Xia, M., Pan, S., Sun, Y., Luo, Q., Fang, Z., He, P., Fu, J., Zhang, Y., 2019. Dehydration behaviours of isopropyl group initiate the surface wettability transition of temperature sensitive poly(*N*-isopropylacrylamide) hydrogel. *Mater. Res. Express* 6, 095704.
- Xiang, Y., Chen, X., Vlassak, J.J., 2005. Plane-strain bulge test for thin films. *J. Mater. Res.* 20, 2360–2370.
- Xie, Y.X., Liu, J.C., Fu, Y.B., 2016. Bifurcation of a dielectric elastomer balloon under pressurized inflation and electric actuation. *Int. J. Solids Struct.* 78–79, 182–188.
- Xu, X., Jagota, A., Hui, C.-Y., 2014. Effects of surface tension on the adhesive contact of a rigid sphere to a compliant substrate. *Soft Matter* 10, 4625–4632.
- Yasuda, H., Sharma, A.K., Yasuda, T., 1981. Effect of orientation and mobility of polymer molecules at surfaces on contact angle and its hysteresis. *J. Polym. Sci.: Polym. Phys. Ed.* 19, 1285–1291.
- Young, T., 1805. III. An essay on the cohesion of fluids. *Philos. Trans. R. Soc. London* 95, 65–87.
- Yue, K., Gao, W., Huang, R., Liechti, K.M., 2012. Analytical methods for the mechanics of graphene bubbles. *J. Appl. Phys.* 112, 083512.
- Zhao, X., Suo, Z., 2008. Method to analyze programmable deformation of dielectric elastomer layers. *Appl. Phys. Lett.* 93, 251902.
- Zhu, J., Cai, S., Suo, Z., 2010. Nonlinear oscillation of a dielectric elastomer balloon. *Polym. Int.* 59, 378–383.